

Manifold Learning Benefits GANs

Yao Ni^{*†}, Piotr Koniusz^{*§†}, Richard Hartley^{†♦}, Richard Nock^{♦♣†}
[†]The Australian National University [§]Data61/CSIRO [♦]Google Research

firstname.lastname@anu.edu.au

Abstract

In this paper¹, we improve Generative Adversarial Networks by incorporating a manifold learning step into the discriminator. We consider locality-constrained linear and subspace-based manifolds², and locality-constrained non-linear manifolds. In our design, the manifold learning and coding steps are intertwined with layers of the discriminator, with the goal of attracting intermediate feature representations onto manifolds. We adaptively balance the discrepancy between feature representations and their manifold view, which is a trade-off between denoising on the manifold and refining the manifold. We find that locality-constrained non-linear manifolds outperform linear manifolds due to their non-uniform density and smoothness. We also substantially outperform state-of-the-art baselines.

1. Introduction

Generative Adversarial Networks (GANs) [13] are powerful models for image generation [5, 19, 22], sound generation [11], image stylization [32] and destylization [46–49], super-resolution [62], feature generation [60, 65], etc. The original GAN learns to generate images [5, 19, 21, 22, 56] by performing the following min-max game:

$$\min_{\theta_G} \max_{\theta_D} \mathcal{J}(D|_{\theta_D}, G|_{\theta_G}), \quad (1)$$

where $\mathcal{J}(\cdot) = \mathbb{E}_{\mathbf{x} \sim p_x(\mathbf{x})} \log(D(\mathbf{x}; \theta_D)) + \mathbb{E}_{z \sim p_z(z)} \log(1 - D(G(z)))$. Eq. (1) updates parameters θ_D of discriminator $D(\mathbf{x}; \theta_D)$ to discriminate between samples from the data distribution $p_x(\mathbf{x})$ and generative distributions $p_g(G)$. Simultaneously, parameters θ_G of generator $G(z; \theta_G)$ are updated to fool the discriminator D . Thus, the noise distribution $p_z(z)$ becomes mapped to $p_x(\mathbf{x})$ via generator G .

However, GANs typically suffer from three problems: **1)** the training instability [25], **2)** the so-called mode collapse [44], and **3)** overfitting of the discriminator [58].

^{*}Equal contribution. Accepted by CVPR 2022.

[♣]Brain team (richardnock@google.com).

¹Code: <https://github.com/MaxwellYaoNi/LCSAGAN>.

²The coding spaces considered in this paper are loosely termed manifolds. In most cases they are not manifolds in the strict mathematical sense, but rather topological spaces such as varieties, or simplicial complexes. The word will be used only in an informal sense.

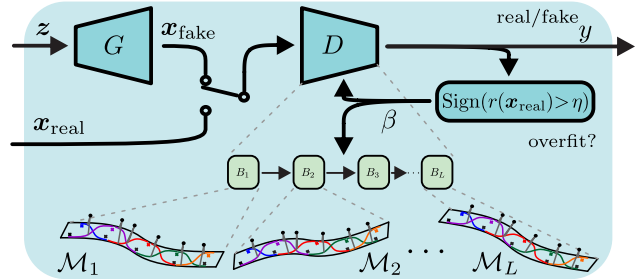


Figure 1. Our GAN pipeline. We equip the discriminator with residual blocks B_1, \dots, B_L , each containing standard CNN operations, e.g. convolutions, ReLU, downsampling, residual link etc., and the manifold learner \mathcal{M}_i . Metaparameter β controls the degree of mixing block conv. features with their view recovered from the manifold. The ‘overfit?’ detector increases β when overfitting to \mathbf{x}_{real} is suspected, which boosts the impact of manifold learners.

The training instability is an imbalanced competition of the generator and the discriminator due to non-overlapping support between the model distribution and the data distribution [6, 19, 25], leading to poor quality of generated data. Mode collapse has to do with sharply rising gradient around undesirable local equilibria [25, 44], resulting in generation of the same image. Finally, discriminator overfitting leads to excessive memorization and poor generalization.

Indeed, with an excessive number of parameters, the discriminator may memorize the training data instead of learning a meaningful distribution, leading to a high real/fake classification accuracy on the training dataset and a low accuracy on the validation split [5, 20, 66]. Webster *et al.* [58] argue such a phenomenon mainly affects the discriminator and is undetectable in the generator, with the exception of hybrid adversarial and non-adversarial methods [4] which impose the so-called consistency loss on a generator.

We also observed discriminator overfitting in baseline models e.g., doubling the number of parameters of discriminator resulted in training and validation FID scores of baseline GANs diverging at some intermediate training stage.

Thus, to reduce overfitting of the discriminator, we propose a data-driven feature manifold-learning step and intertwine it with layers of the discriminator. In this way, the discriminator learns the feature manifold at different levels of object abstraction, from fine to coarse, which limits

the complexity of parameter space and separates the signal from noise as both generated and real data are expressed on a common manifold. As a result, the generator diversifies the generated patterns according to their view on the manifold, on which the discriminator operates. The min-max game operates on a gradually learnt manifold (see Fig. 1).

Our contributions are threefold:

- i. We intertwine locality-constrained and subspace-based feature encoding and dictionary learning steps [29, 34] with blocks of the GAN discriminator to exploit manifold learning in an end-to-end scenario.
- ii. We employ a balancing term to help blocks of the discriminator learn the data-driven manifold from the encoder intertwined with them, while permitting some degree of freedom in the vicinity of that manifold (§2).
- iii. We show that locality-constrained soft assignment coding (the best coder in our experiments) acts as a locally flexible denoiser [1] due to its Lipschitz continuity which we control to vary its operating mode between the ordinary k-means quantization and locality-constrained linear coding. This setting admits quantization of some feature space parts while approximately preserving linearity of other feature space parts (§5).

For contribution (i), we investigate Sparse Coding (SC) [31, 61], Non-negative Sparse Coding (SC₊) [16], Orthogonal Matching Pursuit (OMP) [8, 42], Locality-constrained Linear Coding (LLC) [55], Soft Assignment (SA) [3, 54], and Locality-constrained Soft Assignment (LCSA) [26–29, 34], and Hard Assignment (HA) [7, 51]. We provide formulations and discussion on properties of each coder in §4.

2. Problem Formulation

Figure 1 shows our pipeline (we skip conditional cues for brevity). We build on BigGAN [5], OmniGAN [69], MSG-StyleGAN [18], StyleGAN2 [22] but we equip the discriminator with the manifold learner which is metacontrolled to reduce overfitting. In §C of the supplementary material, we also study the combination of our method with DA [66], ADA [20] and LeCamGAN [53] in limited data scenario.

The discriminator $D(\mathbf{x}; \theta_D)$ of the GAN in Eq. (1) classifies input images as real or fake. Many architectures exist in the literature *e.g.*, GAN [13] uses the discriminator based on a convolutional network, whereas recent architectures *e.g.*, BigGAN [5], OmniGAN [69], MSG-StyleGAN [18] and StyleGAN2 [22] use residual discriminators with L residual blocks *e.g.*, see BigGAN [5] (their Fig. 16).

Let³ $\mathbf{f} : \mathbb{R}^{d \times N} \times \mathbb{R}^{|\theta_B|} \rightarrow \mathbb{R}^{d' \times N'}$ (where $|\theta_B|$ is the size of the set of parameters θ_B) be a function realized by a single discriminator block with parameters θ_B , where d and d' are the number of input/output channels, $N = WH$ and

³Our notations are explained in §A of the supplementary material.

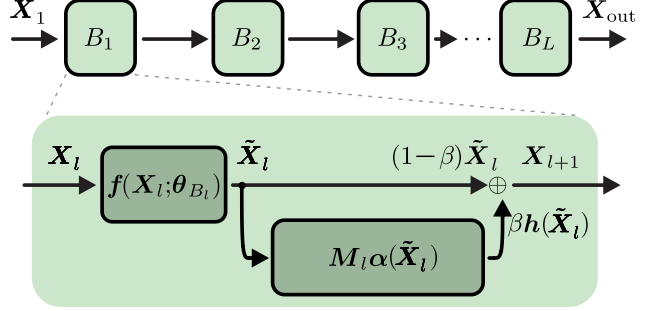


Figure 2. Blocks B_1, \dots, B_L of our discriminator contain a standard block denoted by \mathbf{f} intertwined with the manifold learner. Metaparameter β controls the mixing balance between \mathbf{f} and \mathbf{h} .

$N' = W'H'$ are the number of input/output spatial locations in feature maps of the block. Often, N' may equal N .

We introduce an encoding function $\mathbf{h} : \mathbb{R}^{d' \times N'} \rightarrow \mathbb{R}^{d' \times N'}$ that maps $\mathbb{R}^{d' \times N'}$ into a subset, usually nowhere dense or of small volume in $\mathbb{R}^{d' \times N'}$, which we sometimes refer to as the *feature space*. In the cases we consider this mapping derives from a mapping $\mathbb{R}^{d'} \rightarrow \mathbb{R}^{d'}$ applied independently and equally over the second dimension $\mathbb{R}^{N'}$. The encoding introduces an error, measured by $\|\mathbf{h}(\mathbf{X}) - \mathbf{X}\|_F \leq \epsilon$ where ϵ is called the reconstruction error.

In dictionary-based encoding, the function \mathbf{h} relies on a dictionary $\mathbf{M} = [\mathbf{m}_1, \dots, \mathbf{m}_k] \in \mathbb{R}^{d' \times k}$ containing k column vectors, the so-called dictionary atoms (sometimes called anchors), defining the underlying manifold \mathcal{M} , and $k \gg d'$ ensures the dictionary is overcomplete. Then, after solving the optimization problem,

$$(\alpha, \mathbf{M}) = \arg \min_{\alpha', \mathbf{M}'} \|\mathbf{X} - \mathbf{M}' \alpha'\|_F^2 + \kappa \Omega(\alpha', \mathbf{M}', \mathbf{X}), \quad (2)$$

where $\alpha \equiv [\alpha_1, \dots, \alpha_{N'}] \in \mathbb{R}^{k \times N'}$, the function \mathbf{h} is defined by $\mathbf{h}(\mathbf{X}) = \mathbf{M}\alpha$. Since α depends on \mathbf{X} , we shall commonly write it as $\alpha(\mathbf{X})$. The mapping \mathbf{h} maps $\mathbb{R}^{d'}$ into a subset \mathcal{M} of $\mathbb{R}^{d'}$, that we will call the feature manifold (or simply manifold).

The choice of $\Omega(\alpha', \mathbf{M}', \mathbf{X})$ realizes some desired constraints via regularization (with $\kappa > 0$) for example, $\Omega(\alpha', \mathbf{M}', \mathbf{X}) = \|\alpha'\|_1$ encourages sparsity of α , while $\Omega(\alpha', \mathbf{M}', \mathbf{X}) = \sum_n [\|\mathbf{x}_n - \mathbf{m}_1\|_2^2, \dots, \|\mathbf{x}_n - \mathbf{m}_{k'}\|_2^2]^T \alpha_n$ encourages locality to express each α_n w.r.t. $\text{Span}(\mathbf{m}_1, \dots, \mathbf{m}_{k'})$, where $\mathbf{m}_1, \dots, \mathbf{m}_{k'}$ are the k' nearest neighbors of \mathbf{x}_n .

We intertwine the encoding step with blocks of the discriminator as follows:

$$\mathbf{X}_{l+1} = (1-\beta)\tilde{\mathbf{X}}_l + \beta \mathbf{h}_l(\tilde{\mathbf{X}}_l) \quad (3)$$

where $\tilde{\mathbf{X}}_l = \mathbf{f}(\mathbf{X}_l; \theta_{B_l})$ and \mathbf{h}_l is the encoding function introduced just above, expressed in terms of a dictionary \mathbf{M}_l , whereas $\{\theta_{B_l}\}_{l=1}^L$ and $\{\mathbf{M}_l\}_{l=1}^L$ are parameters of blocks of the discriminator and dictionaries for layers $1, \dots, L$ respectively. Figure 2 illustrates Eq. (3) applied to blocks B_1, \dots, B_L of the discriminator.

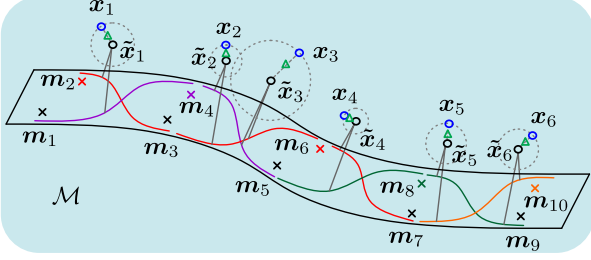


Figure 3. Our manifold setting. Atoms m_1, \dots, m_k (crosses \times) define the geometry of the manifold. Samples $x_1, \dots, x_{N'}$ (blue \circ) are projected onto the manifold \mathcal{M} via function $\alpha(x)$ and then recovered via $h(x)$, which produces recovered samples $\tilde{x}_1, \dots, \tilde{x}_{N'}$ (black \circ). The grey circles indicate L_2 balls imposed by the proximity operator in Eq. (4) while green triangles \triangle are trade-off samples between f and h , controlled by β within L_2 balls. We note that radii of L_2 balls are controlled by γ but each ball can be larger or smaller depending whether this benefits the discrimination loss. Thus, where desired, trade-off samples are refined by f w.r.t. h within L_2 balls. Curly lines (sigmoid-like \smile) indicate we use locally the sigmoid non-linearity.

At the same time, we prevent Eq. (3) from becoming a residual link by adding a reconstruction loss to the GAN objective:

$$\mathcal{J}_{\text{prox}} = \frac{\gamma}{L} \sum_{l=1}^L \epsilon(\tilde{X}_l; M_l), \quad \text{where} \quad (4)$$

$$\epsilon(\tilde{X}_l; M_l) = \|\tilde{X}_l - h_l(\tilde{X}_l)\|_F^2.$$

Metaparameters (β, γ) control the mixing balance and the proximity between f and h .

Meta-adaptation of (β, γ) . Discriminator overfitting can be detected with a hypothesis test on the expectation over decisions $r(\mathbf{x}_{\text{real}}) = \mathbb{E}[\text{Sign}(D(\mathbf{x}_{\text{real}}))]$ w.r.t. samples \mathbf{x}_{real} , defined as $\text{Sign}(r(\mathbf{x}_{\text{real}}) > \eta) \in \{-1, 0, 1\}$, where $\eta = 0.5$ is the threshold whose violation indicates potential overfitting, as the discriminator becomes increasingly good at distinguishing real datapoints [20]. Thus, to update (β, γ) , we apply:

$$\beta_{t+1} = \beta_t + \Delta_\beta \cdot \text{Sign}(r(\mathbf{x}_{\text{real}}) > \eta), \quad (5)$$

$$\gamma_{t+1} = \gamma_0 + \Delta_\gamma \cdot \beta_{t+1}, \quad (6)$$

where $\beta_0 = 0.1$. $\Delta_\beta = 0.001$ ensures a gradual change of β by increasing contributions from $h(\tilde{X}_l)$ in Eq. (3) when overfitting is detected, and increasing contributions from \tilde{X}_l in Eq. (3) when overfitting vanishes. By setting $\gamma_0 = 0.1$, we ensure that the proximity loss in Eq. (4) is always enabled, and $0.01 \leq \Delta_\gamma \leq 3$ controls the strength of proximity.

Discussion. Figure 3 shows our manifold setting, which exploits the interplay between Eq. (3) and Eq. (4). We alternately learn encoding of samples X_l on manifold M_l and refine dictionary M_l . The proximity operator in Eq. (4) encourages samples \tilde{X}_l to stay in the proximity of their recovered view $h(\tilde{X}_l)$ by controlling L_2 balls around $h(\tilde{X}_l)$. Eq. (3) interpolates between $h(\tilde{X}_l)$ and \tilde{X}_l within L_2 balls.

We opt for such a design as (i) f may refine h if the discriminator loss spotting real/fake inputs deems it useful, (ii) h is preferred when overfitting is detected, whereas f introduces refined patterns otherwise, (iii) f is encouraged to learn from the piecewise-smooth h (see §5).

3. Related Works

Modern GANs. Recent GANs build on GAN [13] or DC-GAN [43] by improving generator or discriminator. A residual model [14] was improved by adding a self-attention block [63]. Progressive GAN [19] uses several levels of layers for increasingly finer image resolution. StyleGAN [21] maps the input to an intermediate latent space and controls the generator through adaptive instance normalization (so-called AdaIN). MSG-GAN passes multi-scale gradients from the discriminator to the generator [18].

Improving GANs. To address training instability, mode collapse and overfitting, researchers study (i) loss and distance formulations, (ii) regularization mechanisms and penalties, and (iii) architectural modifications.

Wasserstein GAN (Arjovsky *et al.* [2]) enjoys a good training stability. It was further improved by Gulrajani *et al.* [14] by penalizing the norm of gradient of the critic. Mean & Covariance GAN [38] matches the generated and real data distributions with first- and second-order statistics. A Maximum Mean Discrepancy GAN [33] matches distributions in the Reproducing Kernel Hilbert Space (RKHS).

Spectral Normalization GAN [36] applies normalization on weights to stabilize the discriminator. Spectral Regularization GAN [35] performs detection of so-called spectral collapse. Disconnected Manifold GAN [23] assumes that natural images lie on a union of disjoint manifolds. Feature Quantization GAN (FQGAN) [67] quantizes features of discriminator into a k-means based dictionary. The Denoising Feature Matching GAN [57] encourages proximity between the output of the generator and a denoising auto-encoder.

Our work differs from the Disconnected Manifold GAN which models an entire image distribution as a union of non-explicit manifolds (a collection of generators). FQGAN imposes quantization on features of the discriminator and Denoising Feature Matching GAN learns a denoising auto-encoder on real images to apply it on generated images.

In contrast, we model coarse-to-fine features extracted from multiple blocks of the discriminator, which capture different semantic levels of abstraction. We encourage these features to lie on explicit locality-constrained non-linear manifolds (each block of our discriminator has its own learner). We adaptively control the mixing levels of features and their views recovered from manifolds, and the smoothness of manifolds to prevent overfitting.

Limiting Overfitting. Augmentations (rotations, clipping) [17, 52, 64, 66] can limit overfitting, however, augmentation

artifacts leak into the generated images [20, 68]. Injecting noises into the discriminator [39, 59] via dropout [50] forms an ensemble network, whereas we equip the discriminator with a data-manifold learner whose smoothness we control.

4. Preliminaries

Below, we explain GAN pipelines on which we build, and feature encoding and dictionary learning, our key tools.

4.1. Baseline GANs

BigGAN [5] combines a projection-based loss [37], spectral normalization [36], and self-attention [63]. The projection-based score is a trade-off between a class-wise cosine similarity and a class independent term:

$$s(\mathbf{x}, \mathbf{y}) = \mathbf{y}^T \mathbf{V} D(\mathbf{x}; \boldsymbol{\theta}_D) + \mathbf{f}'(D(\mathbf{x}; \boldsymbol{\theta}_D); \boldsymbol{\theta}_{D'}), \quad (7)$$

where $\mathbf{y} \in \{0, 1\}^C$ and $\|\mathbf{y}\|_1 = 1$, $\mathbf{V} \in \mathbb{R}^{C \times d'}$ is a bilinear compatibility matrix that associates output features \mathbf{X}_{out} from D with the class label. As \mathbf{y} is a one-hot vector, $\mathbf{V} \equiv [\mathbf{v}_1, \dots, \mathbf{v}_C]^T$ contains linear projectors \mathbf{v}_c , one per class $c \in \{0, \dots, C-1\}$. Function $\mathbf{f}' : \mathbb{R}^{d'} \rightarrow 1$ is realized by an FC layer with parameters $\boldsymbol{\theta}_{D'}$. Scores $s(\mathbf{x}, \mathbf{y})$ are passed to a hinge-based loss with two components:

$$\mathcal{J}_{\text{discr}} = \mathbb{E}_{(\mathbf{x}, \mathbf{y}) \sim p_{\mathbf{x} \times \mathbf{y}}^{\text{real}}(\mathbf{x}, \mathbf{y})} \max(0, 1 - s(\mathbf{x}, \mathbf{y})) + \mathbb{E}_{(\mathbf{z}, \mathbf{y}_z) \sim p_{\mathbf{z} \times \mathbf{y}_z}(\mathbf{z}, \mathbf{y}_z)} \max(0, 1 + s(G(\mathbf{z}, \mathbf{y}_z), \mathbf{y}_z)). \quad (8)$$

Our manifold-based pipeline combines loss $\mathcal{J}_{\text{prox}}$ from Eq. (4) with $\mathcal{J}_{\text{discr}}$ and the original \mathcal{J}_{gen} from [5].

OmniGAN [69] uses a multi-label softmax loss (where a label vector $\mathbf{y} \in \{0, 1\}^{C+2}$, $\|\mathbf{y}\|_1 = 2$ is a concatenation of the one-hot class label vector and one-hot real/fake vector):

$$\mathcal{J}_{\text{discr}} = \mathbb{E}_{(\mathbf{x}, \mathbf{y}) \sim p_{\mathbf{x} \times \mathbf{y}}^{\text{real}}(\mathbf{x}, \mathbf{y})} s(\mathbf{x}, \mathbf{y}) + \mathbb{E}_{(\mathbf{z}, \mathbf{y}_z) \sim p_{\mathbf{z} \times \mathbf{y}_z}(\mathbf{z}, \mathbf{y}_z)} s(G(\mathbf{z}, \mathbf{y}_z), \mathbf{y}_z) \quad \text{where} \quad (9)$$

$$s(\mathbf{x}, \mathbf{y}) = \sum_{c=0}^{C+1} \log \left(1 + e^{-\text{Sign}(y_c - 0.5) \phi_c(\mathbf{x})} \right). \quad (10)$$

We note that \mathbf{X}_{out} represents output features from D , $\phi(\mathbf{x}) = \mathbf{f}'(D(\mathbf{x}; \boldsymbol{\theta}_D); \boldsymbol{\theta}_{D'})$, where function $\mathbf{f}' : \mathbb{R}^{d'} \rightarrow C+2$ is realized by an FC layer with parameters $\boldsymbol{\theta}_{D'}$.

4.2. Feature Coding and Dictionary Learning on Data-driven Manifolds

Below, we formalize feature encoding and dictionary learning approaches listed in §1. In experiments, we substitute a chosen coding step into function $\mathbf{h}(\mathbf{x})$ from §2. Moreover, $\mathbf{M} \equiv [\mathbf{m}_1, \dots, \mathbf{m}_k] \in \mathbb{R}^{d' \times k}$ is a dictionary whose learning step is detailed at the bottom of §4.2, and $\boldsymbol{\alpha}(\mathbf{x})$ represents the encoding/mapping on the simplex.

Hard Assignment (HA) [7, 51]. This encoder assigns each \mathbf{x} to its nearest \mathbf{m} by solving the following optimisation problem:

$$\boldsymbol{\alpha}(\mathbf{x}) = \arg \min_{\boldsymbol{\alpha}' \in \{0, 1\}^k} \|\mathbf{x} - \mathbf{M} \boldsymbol{\alpha}'\|_2^2, \quad (11)$$

$$\text{s.t. } \|\boldsymbol{\alpha}'\|_1 = 1.$$

If \mathbf{M} is formed by k-means clustering, HA becomes an equivalent of the quantizer from FQGAN [67].

Sparse Coding (SC) [31, 61] & **Non-negative Sparse Coding (SC₊)** [16]. SC encodes \mathbf{x} as a sparse linear combination of atoms \mathbf{M} by optimising the following objective:

$$\boldsymbol{\alpha}(\mathbf{x}) = \arg \min_{\boldsymbol{\alpha}'} \|\mathbf{x} - \mathbf{M} \boldsymbol{\alpha}'\|_2^2 + \kappa \|\boldsymbol{\alpha}'\|_1, \quad (12)$$

whereas SC₊ additionally imposes a constraint that $\boldsymbol{\alpha}' \geq 0$. Both SC and SC₊ encode \mathbf{x} on a subset of \mathbf{M} of size controlled by the sparsity term.

Orthogonal Matching Pursuit (OMP) [8, 42]. This encoder expresses \mathbf{x} as a sparse linear combination of atoms \mathbf{M} by optimising the following objective:

$$\boldsymbol{\alpha}(\mathbf{x}) = \arg \min_{\boldsymbol{\alpha}'} \|\mathbf{x} - \mathbf{M} \boldsymbol{\alpha}'\|_2^2, \quad (13)$$

$$\text{s.t. } \|\boldsymbol{\alpha}'\|_0 \leq \tau,$$

where the pseudo-norm $\|\boldsymbol{\alpha}'\|_0$ ensures the count of non-zero coefficients of $\boldsymbol{\alpha}'$ is at most τ . Unlike SC and SC₊, $\|\boldsymbol{\alpha}'\|_0$, the penalty enforces a strict limit on the number of non-zero elements in $\boldsymbol{\alpha}'$, but the problem itself is NP-hard.

Approximate Locality-constrained Linear Coding (LLC) [55]. LLC expresses \mathbf{x} as a linear combination of k' nearest neighbor atoms of \mathbf{x} selected from \mathbf{M} , forming subspaces of size k' on a piecewise-linear manifold:

$$\boldsymbol{\alpha}(\mathbf{x}) = \arg \min_{\boldsymbol{\alpha}'} \|\mathbf{x} - \mathbf{M} \boldsymbol{\alpha}'\|_2^2, \quad (14)$$

$$\text{s.t. } \mathbf{1}^T \boldsymbol{\alpha}' = 1,$$

and $\boldsymbol{\alpha}'$ is further constrained by $\alpha'_i = 0$ unless \mathbf{m}_i is one of the k' closest neighbors of \mathbf{x} .

Soft Assignment (SA) [3, 54] & **Locality-constrained Soft Assignment (LCSA)** [26, 29, 34]. SA expresses \mathbf{x} as the membership probability (concept known from GMM [3]) of \mathbf{x} belonging to each \mathbf{m}_i in \mathbf{M} under equal mixing probability and equal variance σ of GMM. SA is given as:

$$\boldsymbol{\alpha}(\mathbf{x}; \mathbf{M}, \sigma) = S_\sigma(\|\mathbf{x} - \mathbf{m}_1\|_2, \dots, \|\mathbf{x} - \mathbf{m}_k\|_2), \quad (15)$$

where S_σ is the softmax function $S_\sigma : \mathbb{R}^k \rightarrow \Delta^{k-1}$, where Δ^{k-1} is the probability simplex and:

$$S_\sigma(d_1, \dots, d_k)_j = \frac{\exp(-d_j^2/2\sigma^2)}{\sum_i \exp(-d_i^2/2\sigma^2)}. \quad (16)$$

This model yields largest values of α'_i for atoms \mathbf{m}_i in \mathbf{M} that are close Euclidean neighbors of \mathbf{x} . However, $\alpha_i(\mathbf{x}) > 0$ even for \mathbf{m}_i that are far from \mathbf{x} . For this reason, SA is not strictly locality-constrained.

LCSA differs from SA by setting $\alpha_i(\mathbf{x}) = 0$ unless \mathbf{m}_i is among the k' nearest-neighbor atoms for \mathbf{x} . The denominator of Eq. (16) performs normalization, that is the summation runs over the k' nearest neighbors. Thus, LCSA maps \mathbb{R}^d onto a set of probability simplices $\Delta^{k'-1}$. As LCSA was the best in our experiments, we analyze it in §5.

Dictionary Learning (DL). For the above coders, we employ a class-agnostic dictionary learning objective which

follows Eq. (2). Let some $\alpha(\mathbf{X}) \equiv [\alpha_1, \dots, \alpha_{N'}]$, then:

$$\mathbf{M} = \arg \min_{\mathbf{M}'} \|\mathbf{X} - \mathbf{M}'\alpha\|_F^2, \quad (17)$$

where \mathbf{M}' can be constrained to contain atoms $\|\mathbf{m}'_i\|_2 \leq 1$ if codes α have non-restricted L_2 norm e.g., for OMP.

Inverse of α . To reproject $\alpha(\mathbf{X})$ from the manifold \mathcal{M} into the Euclidean space, we simply compute $\tilde{\mathbf{X}} = \mathbf{M}\alpha(\mathbf{X})$.

Implementation Remarks. Coding methods, dictionary learning, and their implementations are detailed in §J of the supplementary material. For dictionary learning, we detach \mathbf{X} and α , and run 1 iteration of gradient descent per mini-batch w.r.t. each \mathbf{M} (no big gain for ≥ 2 iterations). For SC and SC+, we detach \mathbf{X} and all \mathbf{M} , and let 5 iterations of gradient descent (no gain for ≥ 6 iterations). LLC has a closed-form solver [55]. Our efficient OMP solves the system of linear equations (no matrix inversion). SA/LCSA enjoy a fast closed-form recipe. LLC and LCSA use the partial sort algorithm for selecting k' nearest neighbors. We detach $\mathbf{M}\alpha$ to compute the proximity loss in Eq. (4).

5. Theoretical Analysis of LCSA

As LCSA is the best encoder in our experiments, we focus on its theoretical properties below. All proofs for theories listed below are in §L of the supplementary material.

In this section, we use the following notation. Suppose a dictionary of atoms $\mathbf{M} = [\mathbf{m}_i]$ in \mathbb{R}^d is given, and $2_{k'}^{\mathbf{M}}$ denotes the set of all subsets of size k' of \mathbf{M} . We define by $\text{NN}_{k'} : \mathbb{R}^d \rightarrow 2_{k'}^{\mathbf{M}}$ to be the set-valued function that takes a point \mathbf{x} to its set of k' nearest neighbor atoms. A maximal subset of \mathbb{R}^d on which $\text{NN}_{k'}(\mathbf{x})$ is constant is called a Voronoi cell. For a given set U in $2_{k'}^{\mathbf{M}}$, then, a Voronoi cell $(\text{NN}_{k'})^{-1}(U)$ is a subset of \mathbb{R}^d consisting of all the points for which U is the set of k' nearest neighbors. The collection of all Voronoi cells constitutes a decomposition of \mathbb{R}^d into disjoint polyhedral regions.

In the case where the set of k' nearest elements of \mathbf{M} is not unique, we leave the set $\text{NN}_{k'}(\mathbf{x})$ undefined. Thus, the Voronoi cells are disjoint open polyhedral regions such that $\text{NN}_{k'}(\mathbf{x})$ is constant on each cell. The complement in \mathbb{R}^d of the set of Voronoi cells is a subset of a finite set of hyperplanes in \mathbb{R}^d .

SA and LCSA encoding. Given a dictionary $\mathbf{M} = [\mathbf{m}_i]$ in \mathbb{R}^d consisting of k' elements, with $k' \leq d+1$, we consider the function $\mathbf{M}\alpha(\mathbf{x})$ where $\alpha(\mathbf{x}) = S_\sigma(\mathbf{x})$ is the softmax mapping Eq. (15). (The dictionary may be the dictionary of k' nearest neighbors of some point \mathbf{x} .)

Proposition 1 *If $\sigma > 0$, the mapping $\mathbf{x} \mapsto \mathbf{M}\alpha(\mathbf{x})$ is a smooth fibration from \mathbb{R}^d onto the interior of the simplex Δ with vertices \mathbf{m}_i . The fibre of this mapping is equal to the linear subspace of \mathbb{R}^d normal to the affine space spanned by the \mathbf{m}_i .*

A fibre is the set of points that map to the same point in $\Delta^{k'-1}$ under this mapping.

Proposition 2 *The following properties of LCSA hold true:*

1. *If $\sigma \rightarrow 0$ or $k' = 1$, the α codes converge to the HA solution (quantization).*
2. *$\alpha(\mathbf{x})$ is an approximately linear coding of \mathbf{x} in the proximity of $\mu(\mathbf{x}) = \frac{1}{k'} \sum_{\mathbf{m}' \in \text{NN}_{k'}(\mathbf{x})} \mathbf{m}'$.*
3. *For \mathbf{x} with nearest neighbor atoms $\{\mathbf{m}_i\} = \text{NN}_{k'}(\mathbf{x})$ with mean $\mu(\mathbf{x})$, and nearest neighbor atom $\mathbf{n}(\mathbf{x}) = \text{NN}_1(\mathbf{x})$, the reconstruction error satisfies*

$$\|\mathbf{M}\alpha(\mathbf{x}) - \mathbf{x}\|_2 \leq \max\left(\|\mathbf{x} - \mathbf{n}(\mathbf{x})\|_2, \|\mathbf{x} - \mu(\mathbf{x})\|_2\right).$$

4. *The reconstruction error varies smoothly on each Voronoi cell. For \mathbf{x} and \mathbf{x}' in the same Voronoi cell and Δ the simplex with vertices $\text{NN}_{k'}(\mathbf{x})$, we have*

- *Local Lipschitz continuity: if $\sigma > 0$, then*

$$\|\mathbf{M}\alpha(\mathbf{x}) - \mathbf{M}\alpha(\mathbf{x}')\| \leq K \|\mathbf{x} - \mathbf{x}'\|$$

where $K = D^2/\sigma^2$ and D is diameter of simplex Δ (the maximum distance between its vertices). The Lipschitz condition holds for $\|\cdot\|_1$ and $\|\cdot\|_2$ norms.

- *The biggest change of the reconstruction error on a Voronoi cell for HA ($\sigma = 0$) is less than or equal to D .*

5. *The LCSA encoding $\mathbf{M}\alpha(\mathbf{x})$ is non-continuous at the boundaries of the Voronoi regions.*

Proposition 3 *Our design fulfils the principles of GAN with Denoising Auto-Encoder (DAE) [1] with loss:*

$$\mathcal{L}_{dae} = \frac{1}{N} \sum_{n=1}^N \left(\|\mathbf{r}(\mathbf{x}_n) - \mathbf{x}_n\|_2^2 + \sigma'^2 \left\| \frac{\partial \mathbf{r}(\mathbf{x})}{\partial \mathbf{x}} \Big|_{\mathbf{x}=\mathbf{x}_n} \right\|_2^2 \right), \quad (18)$$

where $\mathbf{r}(\mathbf{x}_n)$ is the reconstruction of \mathbf{x}_n akin to our $\mathbf{h}(\mathbf{x}_n)$ in Eq. (4). More importantly, σ'^2 specifies the noise variance. Specifically, we note the following:

6. *Not surprisingly, the proximity loss in Eq. (4) fulfils somewhat similar role to $\|\mathbf{r}(\mathbf{x}_n) - \mathbf{x}_n\|_2^2$ in Eq. (18).*
7. *LCSA implicitly fulfils the denoising role (apart from locality-constrained non-linear coding) of $\sigma'^2 \left\| \frac{\partial \mathbf{r}(\mathbf{x})}{\partial \mathbf{x}} \right\|_F^2$, with σ of LCSA and σ' of DAE related i.e., σ'^2 is proportional to our σ^2 . To this end, we notice that DAE penalises the Frobenius norm of the Jacobian matrix $\left\| \frac{\partial \mathbf{r}(\mathbf{x})}{\partial \mathbf{x}} \right\|_F$ by increasing σ'^2 . We penalise the spectral norm of Jacobian matrix $\left\| \frac{\partial \mathbf{M}\alpha(\mathbf{x})}{\partial \mathbf{x}} \right\|_2 = K$ via de facto controlling the Lipschitz constant $K = D^2/\sigma^2$.*

Discussion. The blue box below explains how properties of LCSA contribute to discriminator training, and how they let LCSA inherit the best properties of other coding methods.

LCSA as a trade-off between HA, LLC, SA, DAE.

Prop. 2 and 3 show that LCSA balances extremes of other coders and inherits their best properties. Prop. 2.1 shows LCSA may act as HA (extreme way to guide f). HA is a localized coder with big reconstruction error. In FQGAN, HA stabilized GAN. Prop. 2.2 shows that LCSA may act as LLC (localized linear coder with very low reconstruction error) in the central parts of Voronoi cells (weak way to guide f). Prop. 2.3 shows that large dictionary is bad, making LCSA a ‘free learner’ as f (easy to overfit).

LCSA is locally-adaptive denoiser. Prop. 2.4 shows each Voronoi cell specialises in how much it denoises f based on the Lipschitz constant $K = D^2/\sigma^2$ (diameter D varies in each cell due to the dictionary). Denoising limits high frequencies of signal and its complexity. Prop. 3.7 shows LCSA denoises by DAE-like mechanism.

6. Experiments

We evaluate our method on CIFAR-10 & CIFAR-100 [30] & ImageNet [9] (conditional GAN) and Oxford-102 Flowers [40] and FFHQ [21] (unconditional setting). We show our LCSA harmonizes with BigGAN [5], OmniGAN [69], MSG-StyleGAN [18] and StyleGAN2 [22].

Datasets. CIFAR-10 has 50K and 10K training and testing images (32×32) from 10 classes, whereas CIFAR-100 has 100 categories. ImageNet has 1.2M and 50K training and validation images with 1K classes. We center-crop and downscale its images to 64×64 and 128×128 pixels. Oxford-102 Flowers contains 8K images of 102 fine-grained flower species. We center-crop its images and resize to 256×256 . FFHQ dataset provides 70K human face images at multiple resolutions (we opt for 256×256). Following [20], we augmented the 70K dataset to 140K with x -flips.

Evaluation Metrics. We generate 50K images per dataset to compute the commonly used Inception Score [45] and Fréchet Inception Distance (FID) [15]. Mean/standard dev. are computed over 5 runs, where both reported. We report tFID, computed between 50K generated images and all training images. For CIFAR-10/CIFAR-100/ImageNet, we also compute vFID between 10K/10K/50K generated images and 10K/10K/50K real testing (val. on ImageNet) images. For Oxford-102 Flowers/FFHQ, we calculate FID between 10K/50K fake images and the entire training set.

6.1. Network Architecture and Hyper-parameters

We build on OmniGAN/BigGAN/StyleGAN2 for CIFAR-10. For CIFAR-100/ImageNet (64×64), we experiment with OmniGAN/BigGAN. For ImageNet (128×128), we build upon OmniGAN given OmniGAN consistently outperforms BigGAN. We employ MSG-StyleGAN as our baseline for Oxford-102 Flowers. For FFHQ, we build upon StyleGAN2 (see §I of the supplementary material).

Model	d'	IS \uparrow	tFID \downarrow	vFID \downarrow
BigGAN [†]	256	9.14	7.05	—
FQGAN [†]		9.16	6.16	—
OmniGAN [†]		9.63	5.52	—
CR-GAN		—	—	11.48
ContraGAN		—	—	10.32
ICR-GAN		—	—	9.21
OmniGAN+LCSA		9.88\pm0.02	4.09\pm0.10	8.16\pm0.07
BigGAN	512	9.36	8.16	12.16
FQGAN		9.38	7.65	11.72
OmniGAN		9.70	6.88	10.65
OmniGAN+LCSA		10.02 \pm 0.05	3.36 \pm 0.06	7.40 \pm 0.06
StyleGAN2+ADA		10.14 \pm 0.09	2.42 \pm 0.04	6.54 \pm 0.06
StyleGAN2+ADA+LCSA		10.18\pm0.06	2.32\pm0.05	6.36\pm0.10
OmniGAN+LCSA	1024	10.21\pm0.03	2.94\pm0.02	6.98\pm0.04

Table 1. Results on CIFAR-10. We combine OmniGAN and StyleGAN2+ADA with LCSA. [†] are results collected from [69].

Model	d'	IS \uparrow	tFID \downarrow	vFID \downarrow
BigGAN [†]	256	10.89	10.18	—
FQGAN [†]		10.62	8.23	—
OmniGAN [†]		13.51	8.14	—
TAC-GAN		9.34	7.22	—
OmniGAN+LCSA		13.60\pm0.11	6.24\pm0.09	11.02\pm0.13
BigGAN	512	11.44	10.16	15.24
FQGAN		11.05	7.76	12.70
OmniGAN		12.78	9.13	13.82
OmniGAN+LCSA		13.71\pm0.03	5.22\pm0.10	9.98\pm0.08
OmniGAN+LCSA	1024	13.88\pm0.12	4.97\pm0.09	9.72\pm0.08

Table 2. Comparison of OmniGAN+LCSA with others on CIFAR-100. [†] are results collected from [69].

6.2. Results of Image Generation

The generated images for each dataset are given in §K of the supplementary material.

CIFAR-10. Table 1 shows results on OminGAN+LCSA, which outperforms the baseline OmniGAN by 0.25 and 1.43 on the IS and tFID metrics ($d' = 256$). With $d' = 512$, we outperform OmniGAN by 0.32 and 3.52. We obtain further improvements with $d' = 1024$ while baselines struggle to converge. Comparisons of different models with $d' = 1024$ are in the §B of the supplementary material.

CIFAR-100. Table 2 shows results on OmniGAN+LCSA against the state of the art. For $d' = 256$, our method gains 0.09 and 1.9 on the IS and tFID metrics over the baseline OmniGAN. For $d' = 512$, we outperform OmniGAN by 0.93 and 3.91 (IS and tFID). Further gains are achieved for $d' = 1024$ while other methods struggle to converge. We include TAC-GAN [12] for comparison.

ImageNet (64×64). Table 3 shows that BiGAN+LCSA outperforms BigGAN by 2.97 and 3.01 (tFID & vFID). OmniGAN+LCSA improves OmniGAN by 6.86 and 2.72 (IS & tFID), which is the state of the art in GANs.

ImageNet (128×128). Table 4 shows OmniGAN+LCSA improves OmniGAN by 23.32 and 2.28 (IS & tFID).

Oxford-102 Flowers. Figure 4(a) shows that MSG-StyleGAN+LCSA improves MSG-StyleGAN by 5.46 on FID. Moreover, Figure 4(b) shows that at around iteration

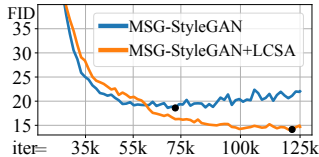
Model	IS \uparrow	tFID \downarrow	vFID \downarrow
Inst. Sel. GAN [10]	43.30	9.07	—
BigGAN	34.50	8.96	8.80
FQGAN	33.14	8.27	8.15
BigGAN+LCSA	33.29	5.99	5.79
OmniGAN	70.59	7.09	7.66
OmniGAN+LCSA	77.45	4.26	4.94

Table 3. Results on ImageNet (64×64). We combine OmniGAN and BigGAN with LCSA. We set $d' = 384$.

Model	IS \uparrow	tFID \downarrow	vFID \downarrow
BigGAN †	104.57	9.19	9.18
OmniGAN †	190.94	8.30	8.93
OmniGAN ‡	169.13	7.11	7.30
OmniGAN+LCSA	192.45	4.83	5.24

Table 4. Results on ImageNet (128×128) with $d' = 384$. † stands for quoting from [69], ‡ are results reproduced by us.

Model	Iters	FID \downarrow
MSG-ProGAN †	53K	28.27
MSG-StyleGAN †	50K	19.60
MSG-StyleGAN	125K	18.59
Ours	125K	13.13



(a) FID of different models.

(b) Training progress.

Figure 4. Results on Oxford-102 Flowers. (a) FID of different models († are results collected from [18]). (b) FID w.r.t. the iteration number for MSG-StyleGAN and MSG-StyleGAN+LCSA on Oxford-102 Flowers. Black dots indicate the minimum FID.

Data	StyleGAN2	+ADA	+LeCam	+bCR	+LCSA	+LCSA+bCR
70k	5.28	4.30	-	3.79	3.83	3.47
140k	3.71	3.81	3.66	3.53	3.32	3.20

Table 5. The FID \downarrow results on FFHQ (256×256) dataset.

number 75K, MSG-StyleGAN starts diverging while MSG-StyleGAN+LCSA (Ours) continues to decrease FID.

FFHQ (256×256). Table 5 shows that StyleGAN2 with LCSA improves the FID of StyleGAN2 by 1.55/0.39 on 70K/140K dataset. Moreover, our LCSA can also be combined with bCR [68] to improve the performance.

Data-limited Generation on CIFAR-10/100. We provide comprehensive experiments (10% and 20% data) in §C of the supplementary material. We summarize our findings as: 1) the augmentation-based ADA [20] and DA [66] leak augmentation artifacts to the generator, while ADA+LCSA and DA+LCSA alleviate this issue (see Figure 24 in the supplementary material). 2) LCSA harmonizes with ADA, DA and LeCam loss [53]. 3) we achieve the state of the art on this limited data setting.

6.3. Impact of Hyperparameters

Below, we conduct ablations on CIFAR-100 for $d' = 512$. **Nearest neighbors k' , σ and k .** Figure 5(a) shows results on OmniGAN+LCSA w.r.t. k' on CIFAR-100, which verifies that the locality-constrained manifold can be constructed with $8 \leq k' \leq 32 \ll k$ with a sufficiently small reconstruction error below the worst case (Prop. 2.3). For

ImageNet, $k' = 8$ also led to best results. Figure 5(b) verifies that $1 \leq \sigma \leq 1.5$ provides the best trade-off in terms of smoothness (quantization vs. linearization) (Prop. 2.1, 2.2 and 2.4). Figure 5(c) verifies the benefit of dictionary overcompleteness $d' \ll k$ as $k = 1024$.

Blocks $l \in \{1, \dots, L\}$ and LCSA. Figure 5(d) shows the results for various combinations of injection of LCSA into blocks of discriminator. It appears that injecting LCSA into all blocks yields the lowest tFID/vFID, which verifies that constructing multiple manifolds at coarse-to-fine semantic level controls the complexity of the discriminator.

Metaparameter β and impact of η . β in Eq. (5) controls the mixing of conv. features obtained by \mathbf{f} and their view \mathbf{h} recovered from the manifold, as in Eq. (3). Figure 6(a) shows that in early iterations, blocks of discriminator learn conv. features. Around 25K iterations, the model starts oscillating between prevention of overfitting and refining conv. features, as indicated by the green curve that continues to gradually grow for $\eta = 0.5$ (c.f. flat curve for $\eta = 0.3$). Figure 6(b) also shows that $\eta = 0.5$ is a universally good threshold.

6.4. Analysis and Ablation studies

We analyse our method on CIFAR-10/100 ($d' = 512$).

Preventing Discriminator Overfitting. Figure 7 verifies that the discriminator of standard methods yields high real/fake accuracy on training images but low accuracy on testing images. Thus, they overfit to the training set (see the large discrepancy between real and fake images). Thus, standard methods diverge early (see FID) but our method continues learning, as shown in Figure 8 and Figure 4(b).

Impact of Different Components. In Table 6, we ablate (i) dictionary learning (Eq. (17)), (ii) the adaptive mixing input Eq. (3) and (iii) proximity loss Eq. (4). We conduct experiments with settings: (1) ACM: removing our manifold learner and the proximity loss, and changing Eq. (3) to be $\mathbf{X}_{l+1} = (1 - \beta)\mathbf{X}_l$ to adaptively control the magnitude of \mathbf{X}_l ; (2) LCSA($\gamma = 0$): removing the proximity loss but keeping the adaptive mixing input; (3) LCSA($\beta = 0$): removing the adaptive mixing input but keeping the adaptive proximity loss; (4) LCSA(EMA): replacing our dictionary learning with the exponential moving average; (5) LCSA(fixed (β, γ)): fixed meta-controller (β, γ) (different combination of (β and γ) is given in §G of the supplementary material). Table 6 shows that (i) LCSA($\gamma = 0$) is better than ACM and OmniGAN which verifies the benefit of adaptive mixing input. (ii) LCSA($\beta = 0$) is better than OmniGAN which verifies the importance of controlling the complexity of learning. (iii) EMA performs worse than our dictionary learning. (iv) As fixed (β, γ) scores lower thus the adaptive meta-controller is useful. In §H (supplementary material), LCSA yields larger errors at foregrounds and smaller at backgrounds, thus intertwining step (mixing in-

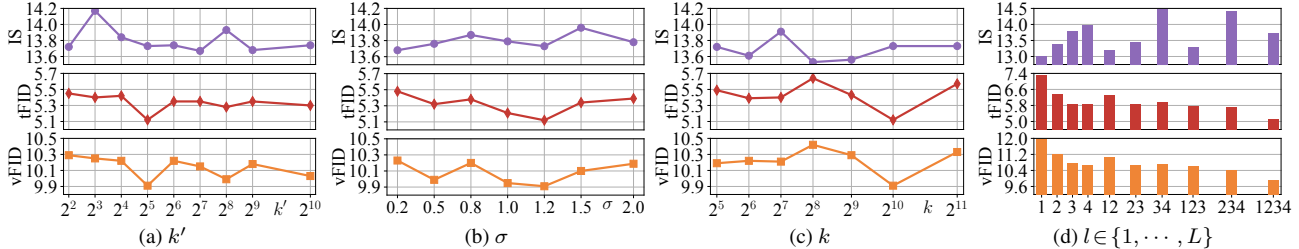


Figure 5. Ablation studies on CIFAR-100 w.r.t. k' (nearest neighbors), σ (controls the Lipschitz constant of LCSA), k (dictionary size), and blocks l which use LCSA. We indicate metrics such as the IS \uparrow , tFID \downarrow and vFID \downarrow .

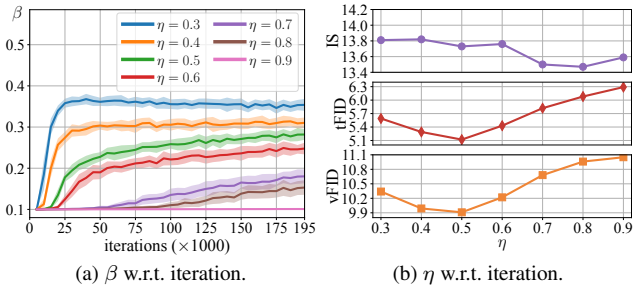


Figure 6. Evolution of metaparameter β and the impact of η which controls the behavior of the detector of overfitting.

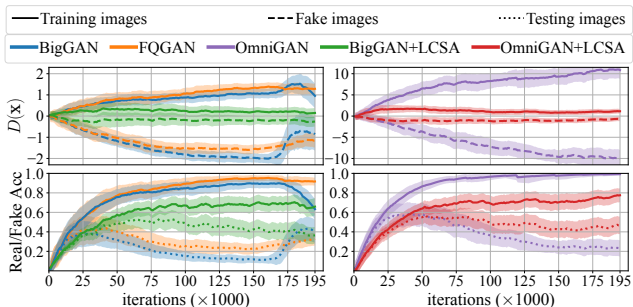


Figure 7. Discriminator predictions on CIFAR-10. We plot the output of discriminator on training images and generated fake images. We test Acc (real/fake accuracy predicted by the discriminator) on the training images and testing images. We use different colors to represent different models. Solid/dash/dot lines indicate training/fake/testing images.

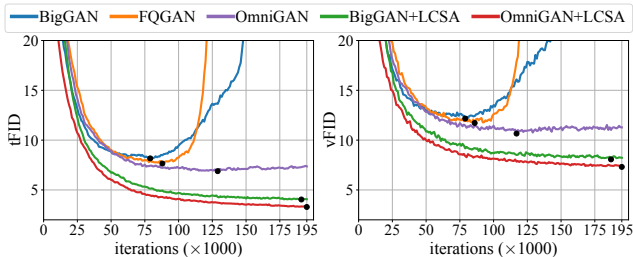


Figure 8. Evolution of tFID and vFID for different models on CIFAR-10. Black dots indicate the minimum FID.

put) helps refine/denoise features before input to next layer.

Different Encoders. Table 6 compares coding methods, each applied to all $l = 1, \dots, 4$ blocks of discriminator. LCSA is the best performer followed by SA and LLC or SC, which validates that using locality-constrained soft as-

Method	CIFAR-10			CIFAR-100		
	IS \uparrow	tFID \downarrow	vFID \downarrow	IS \uparrow	tFID \downarrow	vFID \downarrow
OmniGAN	9.70	6.88	10.65	12.78	9.13	13.82
+ACM	9.79	6.03	9.99	12.82	10.61	15.51
+LCSA($\gamma = 0$)	9.80	5.15	8.35	13.42	8.12	12.78
+LCSA($\beta = 0$)	9.73	4.77	8.77	13.64	5.54	10.37
+LCSA(EMA)	9.91	3.83	7.89	13.71	5.63	10.40
+LCSA(fixed(β, γ))	10.01	4.06	8.03	13.64	5.46	10.29
+LCSA	10.09	3.29	7.31	13.73	5.12	9.91
+HA	9.88	4.52	8.49	13.68	5.52	10.33
+SC+	10.09	3.53	7.65	13.82	5.49	10.31
+SC	10.14	3.48	7.46	13.68	5.40	10.20
+OMP	10.02	3.83	7.83	13.58	5.52	10.40
+LLC	10.04	3.77	7.75	13.61	5.35	10.14
+SA	10.00	3.46	7.45	13.76	5.31	10.19
+DAE	10.08	3.89	7.91	13.65	5.41	10.22

Table 6. Results for ablation studies on CIFAR-10 & CIFAR-100.

signment whose continuity is controlled via the Lipschitz constant (Prop. 2.4) inverse-proportional to σ^2 is more robust than locally-linear coding, due to the quantization vs. linear reconstruction trade-off and the role of σ^2 in denoising (Prop. 3). We also tried replacing the LCSA coder with Denoising Auto-Encoder (DAE) [1] (the setup is in §F of the supplementary material). LCSA achieves better tFID and vFID than locality-constrained linear coding, subspace learning, and DAE. Figure 25 of the supplementary material shows the variance computed over LCSA codes for individual images. While visually mundane regions have low variance (*i.e.*, single code of α encodes it), the visually diverse regions have variance that is somewhat higher for LCSA than other coders, preventing overfitting where it matters.

7. Conclusions

We have applied data-manifold learning (LCSA) in the coarse-to-fine manner to conv. features of discriminator to prevent its overfitting by adaptively balancing the trade-off between denoising on the manifold and refining the manifold (intertwining and dictionary learning steps), controlling the complexity of learning (the proximity loss). Locality-constrained soft assignment is controlled via the Lipschitz constant, resulting in a trade-off between quantization and linear coding, yielding state-of-the-art results.

Acknowledgements. We thank CSIRO’s Machine Learning and Artificial Intelligence Future Science Platform (MLAI FSP) and China Scholarship Council (CSC) for the support.

References

- [1] Guillaume Alain and Yoshua Bengio. What regularized auto-encoders learn from the data-generating distribution. *JMLR*, 15(110):3743–3773, 2014. 2, 5, 8, 11, 13
- [2] Martin Arjovsky, Soumith Chintala, and Léon Bottou. Wasserstein generative adversarial networks. In *ICML*, pages 214–223, 2017. 3
- [3] Jeff A Bilmes. A Gentle Tutorial of the EM Algorithm and its Application to Parameter Estimation for Gaussian Mixture and Hidden Markov Models. Technical report, 1998. 2, 4
- [4] Piotr Bojanowski, Armand Joulin, David Lopez-Pas, and Arthur Szlam. Optimizing the latent space of generative networks. In *ICML*, volume 80, pages 600–609, 2018. 1
- [5] Andrew Brock, Jeff Donahue, and Karen Simonyan. Large scale GAN training for high fidelity natural image synthesis. In *ICLR*, 2019. 1, 2, 4, 6, 14
- [6] Casey Chu, Kentaro Minami, and Kenji Fukumizu. Smoothness and stability in gans. In *ICLR*, 2020. 1
- [7] Gabriella Csurka, Christopher Dance, Lixin Fan, Jutta Willamowski, and Cédric Bray. Visual categorization with bags of keypoints. In *Workshop on statistical learning in computer vision, ECCV*, 2004. 2, 4
- [8] Geoffrey Davis, Stéphane Mallat, and Zhifeng Zhang. Adaptive time-frequency decompositions with matching pursuits. *Optical Engineering*, 33, 1994. 2, 4
- [9] Jia Deng, Wei Dong, Richard Socher, Li-Jia Li, Kai Li, and Li Fei-Fei. Imagenet: A large-scale hierarchical image database. In *CVPR*, pages 248–255, 2009. 6, 11
- [10] Terrance DeVries, Michal Drozdal, and Graham W Taylor. Instance selection for gans. *NeurIPS*, 2020. 7
- [11] Chris Donahue, Julian McAuley, and Miller Puckette. Adversarial audio synthesis. In *ICLR*, 2019. 1
- [12] Mingming Gong, Yanwu Xu, Chunyuan Li, Kun Zhang, and Kayhan Batmanghelich. Twin auxiliary classifiers gan. In H. Wallach, H. Larochelle, A. Beygelzimer, F. d’Alché-Buc, E. Fox, and R. Garnett, editors, *NeurIPS*, pages 1330–1339, 2019. 6
- [13] Ian Goodfellow, Jean Pouget-Abadie, Mehdi Mirza, Bing Xu, David Warde-Farley, Sherjil Ozair, Aaron Courville, and Yoshua Bengio. Generative adversarial nets. In *NeurIPS*, 2014. 1, 2, 3
- [14] Ishaan Gulrajani, Faruk Ahmed, Martin Arjovsky, Vincent Dumoulin, and Aaron Courville. Improved training of wasserstein gans. In *NeurIPS*, pages 5769–5779, 2017. 3
- [15] Martin Heusel, Hubert Ramsauer, Thomas Unterthiner, Bernhard Nessler, and Sepp Hochreiter. Gans trained by a two time-scale update rule converge to a local nash equilibrium. In *NeurIPS*, volume 30, pages 6626–6637, 2017. 6
- [16] Patrik O Hoyer. Non-negative sparse coding. In *Proceedings of the 12th IEEE workshop on neural networks for signal processing*, pages 557–565. IEEE, 2002. 2, 4
- [17] Jongheon Jeong and Jinwoo Shin. Training {gan}s with stronger augmentations via contrastive discriminator. In *ICLR*, 2021. 3
- [18] Animesh Karnewar and Oliver Wang. Msg-gan: Multi-scale gradients for generative adversarial networks. In *CVPR*, pages 7799–7808, 2020. 2, 3, 6, 7, 14
- [19] Tero Karras, Timo Aila, Samuli Laine, and Jaakko Lehtinen. Progressive growing of GANs for improved quality, stability, and variation. In *ICLR*, 2018. 1, 3
- [20] Tero Karras, Miika Aittala, Janne Hellsten, Samuli Laine, Jaakko Lehtinen, and Timo Aila. Training generative adversarial networks with limited data. *NeurIPS*, 33, 2020. 1, 2, 3, 4, 6, 7, 11, 12, 14
- [21] Tero Karras, Samuli Laine, and Timo Aila. A style-based generator architecture for generative adversarial networks. In *CVPR*, 2019. 1, 3, 6, 23
- [22] Tero Karras, Samuli Laine, Miika Aittala, Janne Hellsten, Jaakko Lehtinen, and Timo Aila. Analyzing and improving the image quality of stylegan. In *CVPR*, pages 8110–8119, 2020. 1, 2, 6
- [23] Mahyar Khayatkhoei, Ahmed Elgammal, and Maneesh Singh. Disconnected manifold learning for generative adversarial networks. In *NeurIPS*, pages 7354–7364, 2018. 3
- [24] Diederik P Kingma and Jimmy Ba. Adam: A method for stochastic optimization. *arXiv:1412.6980*, 2014. 14
- [25] Naveen Kodali, Jacob Abernethy, James Hays, and Zolt Kira. On convergence and stability of gans. *arXiv:1705.07215*, 2017. 1
- [26] Piotr Koniusz and Krystian Mikolajczyk. Soft Assignment of Visual Words as Linear Coordinate Coding and Optimisation of its Reconstruction Error. *ICIP*, 2011. 2, 4
- [27] Piotr Koniusz, Fei Yan, Philippe-Henri Gosselin, and Krystian Mikolajczyk. Higher-order Occurrence Pooling on Mid- and Low-level Features: Visual Concept Detection. Technical report, INRIA, Sept. 2013. 2
- [28] Piotr Koniusz, Fei Yan, Philippe-Henri Gosselin, and Krystian Mikolajczyk. Higher-order occurrence pooling for bags-of-words: Visual concept detection. *TPAMI*, 2016. 2
- [29] Piotr Koniusz, Fei Yan, and Krystian Mikolajczyk. Comparison of Mid-Level Feature Coding Approaches And Pooling Strategies in Visual Concept Detection. *CVIU*, 2012. 2, 4
- [30] Alex Krizhevsky. Learning multiple layers of features from tiny images. Technical report, 2009. 6, 11
- [31] Honglak Lee, Alexis Battle, Rajat Raina, and Andrew Ng. Efficient sparse coding algorithms. *NeurIPS*, pages 801–808, 2006. 2, 4
- [32] Chuan Li and Michael Wand. Precomputed real-time texture synthesis with markovian generative adversarial networks. In *ECCV*, 2016. 1
- [33] Chun-Liang Li, Wei-Cheng Chang, Yu Cheng, Yiming Yang, and Barnabas Poczos. Mmd gan: Towards deeper understanding of moment matching network. In *NeurIPS*, volume 30, pages 2203–2213, 2017. 3
- [34] Liu Lingqiao, Lei Wang, and Xinwang Liu. In Defence of Soft-assignment Coding. *ICCV*, 2011. 2, 4
- [35] Kanglin Liu, Wenming Tang, Fei Zhou, and Guoping Qiu. Spectral regularization for combating mode collapse in gans. In *ICCV*, pages 6382–6390, 2019. 3
- [36] Takeru Miyato, Toshiki Kataoka, Masanori Koyama, and Yuichi Yoshida. Spectral normalization for generative adversarial networks. In *ICLR*, 2018. 3, 4
- [37] Takeru Miyato and Masanori Koyama. cgans with projection discriminator. In *ICLR*, 2018. 4

- [38] Youssef Mroueh, Tom Sercu, and Vaibhava Goel. Mcgan: Mean and covariance feature matching gan. In *ICML*, pages 2527–2535, 2017. [3](#)
- [39] Yao Ni, Dandan Song, Xi Zhang, Hao Wu, and Lejian Liao. Cagan: Consistent adversarial training enhanced gans. In *IJCAI*, pages 2588–2594, 2018. [4](#)
- [40] Maria-Elena Nilsback and Andrew Zisserman. Automated flower classification over a large number of classes. In *ICVGIP*, pages 722–729. IEEE, 2008. [6](#)
- [41] Dylan M. Paiton, David Schultheiss, Matthias Kuehmerer, Zac Cranko, and Matthias Bethge. The geometry of adversarial subspaces, 2022. [27](#)
- [42] Yagyensh Chandra Pati, Ramin Rezaifar, and Perinkulam Sambamurthy Krishnaprasad. Orthogonal matching pursuit: Recursive function approximation with applications to wavelet decomposition. In *ACSSC*, pages 40–44, 1993. [2, 4](#)
- [43] Alec Radford, Luke Metz, and Soumith Chintala. Unsupervised representation learning with deep convolutional generative adversarial networks. *arXiv:1511.06434*, 2015. [3](#)
- [44] Kevin Roth, Aurelien Lucchi, Sebastian Nowozin, and Thomas Hofmann. Stabilizing training of generative adversarial networks through regularization. *arXiv:1705.09367*, 2017. [1](#)
- [45] Tim Salimans, Ian Goodfellow, Wojciech Zaremba, Vicki Cheung, Alec Radford, Xi Chen, and Xi Chen. Improved techniques for training gans. In *NeurIPS*, pages 2234–2242. 2016. [6](#)
- [46] Fatemeh Shiri, Xin Yu, Piotr Koniusz, and Fatih Porikli. Face destylization. In *DICTA*, pages 1–8. IEEE, 2017. [1](#)
- [47] Fatemeh Shiri, Xin Yu, Fatih Porikli, Richard Hartley, and Piotr Koniusz. Identity-preserving face recovery from portraits. In *WACV*, 2018. [1](#)
- [48] Fatemeh Shiri, Xin Yu, Fatih Porikli, Richard Hartley, and Piotr Koniusz. Identity-preserving face recovery from stylized portraits. *IJCV*, 127(6-7):863–883, 2019. [1](#)
- [49] Fatemeh Shiri, Xin Yu, Fatih Porikli, Richard Hartley, and Piotr Koniusz. Recovering faces from portraits with auxiliary facial attributes. In *WACV*, pages 406–415, 2019. [1](#)
- [50] Nitish Srivastava, Geoffrey Hinton, Alex Krizhevsky, Ilya Sutskever, and Ruslan Salakhutdinov. Dropout: a simple way to prevent neural networks from overfitting. *JMLR*, 15(1):1929–1958, 2014. [4](#)
- [51] Hugo Steinhaus. Sur la division des corps matériels en parties. *Bull. Acad. Pol. Sci., Cl. III*, 4:801–804, 1957. [2, 4](#)
- [52] Ngoc-Trung Tran, Viet-Hung Tran, Ngoc-Bao Nguyen, Trung-Kien Nguyen, and Ngai-Man Cheung. On data augmentation for gan training. *TIP*, 30:1882–1897, 2021. [3](#)
- [53] Hung-Yu Tseng, Lu Jiang, Ce Liu, Ming-Hsuan Yang, and Weilong Yang. Regularizing generative adversarial networks under limited data. In *CVPR*, 2021. [2, 7, 12](#)
- [54] Jan van Gemert, Jan-Mark Geusebroek, Cor Veenman, and Arnold Smeulders. Kernel Codebooks for Scene Categorization. *ECCV*, 5304:696–709, 2008. [2, 4](#)
- [55] Jinjun Wang, Jianchao Yang, Kai Yu, Fengjun Lv, Thomas Huang, and Yihong Gong. Locality-constrained linear coding for image classification. In *CVPR*, pages 3360–3367, 2010. [2, 4, 5](#)
- [56] Ting-Chun Wang, Ming-Yu Liu, Jun-Yan Zhu, Andrew Tao, Jan Kautz, and Bryan Catanzaro. High-resolution image synthesis and semantic manipulation with conditional gans. In *CVPR*, pages 8798–8807, 2018. [1](#)
- [57] David Warde-Farley and Yoshua Bengio. Improving generative adversarial networks with denoising feature matching. 2016. [3](#)
- [58] Ryan Webster, Julien Rabin, Loic Simon, and Frederic Jurie. Detecting overfitting of deep generative networks via latent recovery. In *CVPR*, 2019. [1](#)
- [59] Xiang Wei, Zixia Liu, Liqiang Wang, and Boqing Gong. Improving the improved training of wasserstein gans. *ICLR*, 2018. [4](#)
- [60] Yongqin Xian, Tobias Lorenz, Bernt Schiele, and Zeynep Akata. Feature generating networks for zero-shot learning. In *CVPR*, 2018. [1](#)
- [61] Jianchao Yang, Kai Yu, Yihong Gong, and Thomas Huang. Linear spatial pyramid matching using sparse coding for image classification. In *CVPR*, pages 1794–1801, 2009. [2, 4](#)
- [62] Xin Yu, Basura Fernando, Bernard Ghanem, Fatih Porikli, and Richard Hartley. Face super-resolution guided by facial component heatmaps. In *ECCV*, pages 217–233, 2018. [1](#)
- [63] Han Zhang, Ian Goodfellow, Dimitris Metaxas, and Augustus Odena. Self-attention generative adversarial networks. In *ICML*, pages 7354–7363, 2019. [3, 4](#)
- [64] Han Zhang, Zizhao Zhang, Augustus Odena, and Honglak Lee. Consistency regularization for generative adversarial networks. In *ICLR*, 2020. [3](#)
- [65] Ruixiang Zhang, Tong Che, Zoubin Ghahramani, Yoshua Bengio, and Yangqiu Song. Metagan: An adversarial approach to few-shot learning. In *NeurIPS*, volume 31, pages 2365–2374, 2018. [1](#)
- [66] Shengyu Zhao, Zhijian Liu, Ji Lin, Jun-Yan Zhu, and Song Han. Differentiable augmentation for data-efficient gan training. *NeurIPS*, 33, 2020. [1, 2, 3, 7, 11, 12](#)
- [67] Yang Zhao, Chunyuan Li, Ping Yu, Jianfeng Gao, and Changyou Chen. Feature quantization improves gan training. In *ICML*, pages 11376–11386, 2020. [3, 4, 14](#)
- [68] Zhengli Zhao, Sameer Singh, Honglak Lee, Zizhao Zhang, Augustus Odena, and Han Zhang. Improved consistency regularization for gans. In *AAAI*, volume 35, pages 11033–11041, 2021. [4, 7](#)
- [69] Peng Zhou, Lingxi Xie, Bingbing Ni, Cong Geng, and Qi Tian. Omni-gan: On the secrets of cgans and beyond. In *ICCV*, pages 14061–14071, 2021. [2, 4, 6, 7, 14](#)

Manifold Learning Benefits GANs (Supplementary Material)

Yao Ni^{*,†}, Piotr Koniusz^{*,§,†}, Richard Hartley^{†,♦}, Richard Nock^{♦,♣,†}
†The Australian National University §Data61/CSIRO ♦Google Research

firstname.lastname@anu.edu.au

Below is the contents of our supplementary material:

- §A explains our mathematical notation.
- §B provides further evaluations on CIFAR-10 and CIFAR-100 (32×32) datasets [30] given the large feature size of $d' = 1024$. We believe that it is valuable to demonstrate that our method can benefit from such a large d' while other methods cannot benefit much when applying $d' = 1024$ instead of the usual $d' = 512$.
- §C provides results for the limited data setting on CIFAR-10 and CIFAR-100.
- §D provides results on the ImageNet (32×32) dataset [9] in order to demonstrate that our LCSA-based pipeline benefits experiments on GAN for lower resolution images, which are favoured over high resolution images for instance when enriching training datasets of few-shot learning approaches. Note that results on ImageNet (64×64) and ImageNet (128×128) are given in our main submission.
- §E explains why FQGAN suffers from discriminator overfitting.
- Section F investigates the use of Denoising Auto-Encoder (DAE) [1] in place of LCSA, and concludes that LCSA is more beneficial.
- §G investigates the use of fixed β and γ rather than metaoptimized β and γ . The conclusion is that with mixing and proximity operators controlled by these parameters, we can reduce overfitting in the discriminator while training the manifold dictionary.
- §H illustrates the residual error between $\tilde{\mathbf{X}}$ and $h(\tilde{\mathbf{X}})$. The results support our belief that conv. encoder refines LCSA on difficult foreground objects while generating coarse-to-fine cov. features close to the manifold.

- §I details hyperparameters used in our experiments. We point out that the majority of parameters remain unchanged throughout many experiments.
- §J provides details of the feature encoding methods and the dictionary learning step.
- §K illustrates examples of images generated with or without the LCSA coder.
- §L offers proofs for claims of §5.

A. Notations

Capitalized boldface symbols are matrices (*e.g.*, \mathbf{X}), lowercase boldface symbols are vectors (*e.g.*, \mathbf{x}), and regular fonts denote scalars *e.g.*, $n, N, l, L, X_{i,j}$ is a (i, j) -th coefficient of \mathbf{X} , x_i is an i -th coefficient of \mathbf{x} . We define a vector of all-ones as $\mathbf{1} = [1, \dots, 1]^T$ and concatenation of α_i as $[\alpha_i]_{i=1, \dots, I}$.

B. Experiments on CIFAR-10/100 ($d' = 1024$)

Below we demonstrate that utilizing LCSA in BigGAN and OmniGAN further enables them to utilize large feature sizes ($d' = 1024$), improving results further. Original BigGAN and OmniGAN struggle to attain good results for such a large feature size. Tables 7 verifies our pipelines on CIFAR-10 and CIFAR-100. Figures 9 and 10 show that our BigGAN+LCSA and OmniGAN+LCSA continue to learn while other models struggle to converge.

Model	CIFAR-10			CIFAR-100		
	IS \uparrow	tFID \downarrow	vFID \downarrow	IS \uparrow	tFID \downarrow	vFID \downarrow
BigGAN	9.64	10.71	14.86	11.54	15.11	19.97
FQGAN	9.44	12.59	16.69	11.74	8.49	13.51
BigGAN+LCSA	9.81	3.51	7.55	11.60	5.49	10.37
OmniGAN	9.92	12.11	16.29	12.42	10.11	14.85
OmniGAN+LCSA	10.21	2.94	6.98	13.88	4.97	9.72

Table 7. Results for different models on CIFAR-10 and CIFAR-100 with $d' = 1024$.

C. Data-limited Generation on CIFAR-10/100

Both DA [66] and ADA [20] limit discriminator overfitting by augmenting the real and generated images that are

*Equal contribution. Accepted by CVPR 2022.

♣Brain team (richardnock@google.com).

Model	CIFAR-10						CIFAR-100					
	100%		20%		10%		100%		20%		10%	
	IS \uparrow / tFID \downarrow / vFID \downarrow	IS \uparrow / tFID \downarrow / vFID \downarrow	IS \uparrow / tFID \downarrow / vFID \downarrow	IS \uparrow / tFID \downarrow / vFID \downarrow	IS \uparrow / tFID \downarrow / vFID \downarrow	IS \uparrow / tFID \downarrow / vFID \downarrow	IS \uparrow / tFID \downarrow / vFID \downarrow	IS \uparrow / tFID \downarrow / vFID \downarrow	IS \uparrow / tFID \downarrow / vFID \downarrow	IS \uparrow / tFID \downarrow / vFID \downarrow	IS \uparrow / tFID \downarrow / vFID \downarrow	IS \uparrow / tFID \downarrow / vFID \downarrow
BigGAN($d' = 256$)	9.26 / 5.46 / 9.38	8.70 / 16.25 / 20.37	8.20 / 31.42 / 35.58	10.99 / 7.89 / 12.74	9.94 / 25.96 / 30.89	7.54 / 50.89 / 55.15						
+DA	9.39 / 4.47 / 8.58	8.95 / 9.38 / 13.26	8.65 / 18.35 / 22.04	10.91 / 7.30 / 11.99	9.73 / 16.32 / 20.88	9.33 / 27.01 / 31.32						
+LeCam	9.48 / 4.25 / 8.27	8.96 / 11.32 / 15.25	8.50 / 26.30 / 30.55	11.44 / 6.53 / 11.23	10.00 / 20.82 / 25.77	8.10 / 39.33 / 44.23						
+LCSA	9.51 / 4.12 / 8.20	8.99 / 8.72 / 12.73	8.74 / 12.36 / 16.46	11.02 / 6.38 / 11.13	10.38 / 13.22 / 18.06	10.08 / 21.13 / 25.87						
+LeCam+DA	9.47 / 4.29 / 8.29	9.05 / 7.53 / 11.46	8.84 / 12.15 / 15.92	11.15 / 6.55 / 11.34	10.42 / 13.01 / 17.65	9.92 / 21.73 / 26.19						
+LCSA+DA	9.50 / 3.75 / 7.83	9.08 / 7.29 / 11.31	8.86 / 10.86 / 14.78	11.21 / 5.76 / 10.52	10.55 / 12.03 / 16.92	10.68 / 19.38 / 24.21						
+LCSA+LeCam+DA	9.47 / 3.80 / 7.89	9.04 / 6.95 / 10.95	8.96 / 10.05 / 13.88	11.17 / 5.85 / 10.64	10.67 / 10.16 / 15.00	10.28 / 18.24 / 23.12						
OmniGAN($d' = 1024$)	9.98 / 6.89 / 10.76	8.62 / 37.86 / 42.18	6.59 / 54.04 / 58.71	12.61 / 8.43 / 13.21	10.11 / 40.57 / 44.86	6.87 / 63.41 / 67.46						
+DA	10.10 / 4.26 / 8.15	9.47 / 13.56 / 17.34	8.96 / 19.59 / 23.60	12.96 / 7.48 / 12.11	11.42 / 17.72 / 22.49	10.21 / 32.61 / 36.86						
+ADA	10.27 / 5.03 / 9.15	9.44 / 27.20 / 31.05	7.72 / 41.82 / 45.36	13.47 / 6.13 / 10.88	12.18 / 13.66 / 18.34	8.81 / 46.74 / 51.03						
+LCSA	10.20 / 2.58 / 6.65	9.97 / 5.15 / 9.01	9.74 / 7.66 / 11.47	13.74 / 4.94 / 9.67	12.86 / 11.15 / 15.90	11.85 / 13.82 / 18.56						
+LCSA+DA	10.22 / 2.52 / 6.60	9.93 / 5.01 / 8.89	9.75 / 7.46 / 11.35	13.79 / 4.58 / 9.46	12.92 / 11.06 / 15.73	11.88 / 13.68 / 18.44						
+LCSA+ADA	10.38 / 2.35 / 6.38	10.12 / 4.48 / 8.41	10.04 / 6.45 / 10.39	13.80 / 4.07 / 8.90	13.78 / 7.45 / 12.11	12.67 / 10.18 / 14.87						

Table 8. Comparison of our LCSA with DA, ADA and LeCam on CIFAR-10 and CIFAR-100 given different percentage of training data.

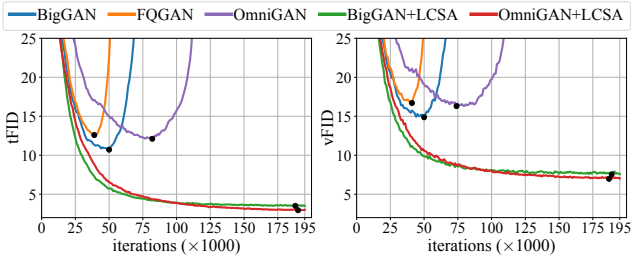


Figure 9. Evolution of tFID and vFID for different models on CIFAR-10 with $d' = 1024$. Black dots indicate the minimum FID.

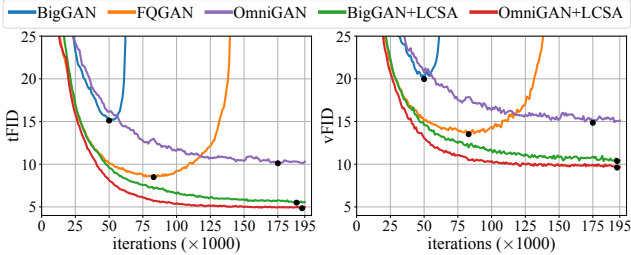


Figure 10. Evolution of tFID and vFID for different models on CIFAR-100 with $d' = 1024$. Black dots indicate the minimum FID.

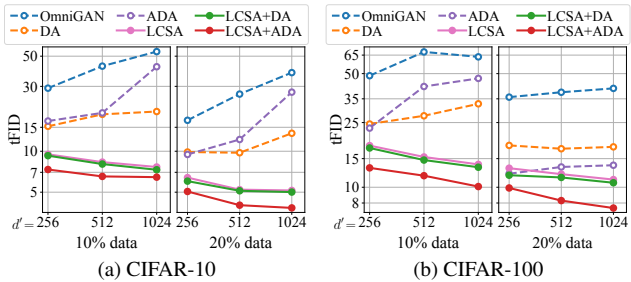


Figure 11. tFID w.r.t. different d' on CIFAR-10 and CIFAR-100 under the limited data setting.

passed to the discriminator. However, in case of DA and ADA, augmentation artifacts leak into the generated images as shown in Figure 24. The LeCamGAN [53] restricts discriminator overfitting by reducing the real/fake loss discrepancy

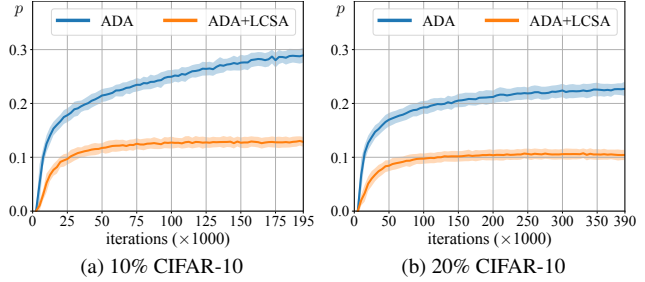


Figure 12. Augmentation strength (p) of ADA vs. ADA+LCSA during training on 10%/20% CIFAR-10 data (OmniGAN $d' = 256$).

at the output of the discriminator. However, it is not enough to limit overfitting by just operating at the output of the discriminator (otherwise a well-designed loss would deal with all overfitting issues which is not the case in the literature). Therefore, we prevent the discriminator overfitting by modifying its blocks by encoding both the features of real and fake images into a common manifold and recovering their view from it, which has the ability to control the complexity of our feature space.

Below, we compare our LCSA with DA [66], ADA [20] on OmniGAN (and/or BigGAN) to variants without LCSA. We conduct experiments based on BigGAN to compare our LCSA with LeCamGAN [53] due to the issue of combining LeCam loss [53] with the multi-output loss of OmniGAN. Following [66], we augmented the real images with x -flip, and trained the OmniGAN and BigGAN for 1K epochs on the full data and 5K epochs on 10%/20% data setting. The DiffAug used translation and cutout augmentations. The ADA used 18 augmentations, including rotations and scaling. Details can be found in [20].

Table 8 shows that our LCSA outperforms DA, ADA and LeCamGAN. LCSA can be always combined with them to improve their performance. Specifically, we achieve state-of-the-art results on CIFAR-10 (100%, 20% and 10%) and CIFAR-100 (20% and 10%) based on OmniGAN ($d' = 1024$). In addition, in Figure 11, OmniGAN, DA and ADA become worse when increasing the d' , while com-

binning them with our LCSA improves the tFID given the larger model size, on which the discriminator can memorize the training data easier, demonstrating that our LCSA has stronger performance while preventing overfitting better than ADA and DA alone. Moreover, we find that the DA and ADA leak the augmentation cues to the generated images, as shown in Figure 24, indicating that their discriminators overfit to the augmentation cues instead of learning meaningful discrimination boundary. ADA strives to control the strength of augmentations by a controller which observes the discriminator output and adjusts the desired augmentation strength. Thus, in Figure 12 we plot the augmentation strength of ADA and LCSA+ADA. We notice that **LCSA+ADA is able to limit the augmentation strength of ADA, thus reducing the leakage of augmentation artifacts**. This means LCSA can deal with the discriminator overfitting well. Concluding, LCSA enjoys better performance than ADA, DA, and LeCam for data-limited generation. LCSA gains further improvements with larger model size d' , and LCSA lowers the risk of leaking augmentation artifacts. Thus, LCSA appears to have the superior capability of preventing discriminator overfitting than other strategies.

D. Experiments on ImageNet (32×32)

We preprocess images by center-cropping and downscaling them to 32 × 32 pixels. We train the network for 100 epochs. We set mini-batch size to 64, $\beta_0 = 0.$, $\gamma_0 = 0.1$, $\eta = 0.5$, $\sigma = 1.2$, whereas the dictionary learning rate is set to 1e-3. We equip each residual block of the discriminator with our LCSA module. We set $\Delta_\gamma = 1.2$ for $d' = 512$. For OmniGAN and OmniGAN+LCSA, we set weight decay of discriminator to be 1e-4 given $d' = 512$. Table 9 presents our results in the above setting.

Model	IS \uparrow	tFID \downarrow	vFID \downarrow
BigGAN	13.25	5.44	5.60
BigGAN+LCSA	13.61	4.82	5.01
OmniGAN	29.55	3.74	4.56
OmniGAN+LCSA	30.53	3.53	4.37

Table 9. Results for ImageNet (32×32).

E. A difference between FQGAN and Hard Assignment

As we note in §4.2, if M is formed by k-means clustering, Hard Assignment becomes an equivalent of the quantizer from FQGAN. However, the FQGAN suffers from discriminator overfitting, as we shown in Figures 8, 9 and 10. The FQGAN uses the proximity loss Eq(4), however, it has no intertwining step between the manifold learning step with blocks of discriminator. That is, for FQGAN, the feature input to the next layer from our pipeline Eq(3) is changed to:

$$\tilde{X}_{l+1} = \tilde{X}_l \quad (19)$$

Without the intertwining step, without the adaptive mechanism, and without LCSA, the FQGAN cannot prevent blocks in discriminator from over-expressing the learned features, which may lie outside of the manifold, resulting in discriminator overfitting.

F. Replacing LCSA with Denoising Auto-Encoder (DAE)

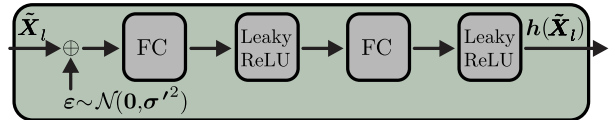


Figure 13. Architecture of DAE. We plug DAE in place of LCSA in Figure 2: we replace $h(\cdot)$ based on LCSA with $h(\cdot)$ based on DAE.

We conduct experiments in which we replace the LCSA coder with Denoising Auto-Encoder(DAE) [1]. As illustrated in Figure 13, two FC layers, each intertwined with LeakyReLU, form our DAE module. Moreover, we apply the mixing mechanism from Eq. (3) and the proximity operator from Eq. (4) which is an equivalent of the reconstruction loss of DAE given in Eq. (18). As Figure 13 indicates, DAE is equipped with a noise injector $\varepsilon \sim \mathcal{N}(\mathbf{0}, \sigma'^2)$ with variance σ'^2 (equivalent in Eq. (18)). We use the multivariate normal distribution which produces noise samples ε that are added to X'_l , while σ'^2 is a vector of on-diagonals equal σ'^2 (off-diagonal coefficients equal 0).

Instead of k (dictionary size), we vary the size of FC layers ($d' \times k_*$) and ($k_* \times d'$), by varying the size of hidden representation k_* . We investigate $k_* \in \{8, 16, 32, 64, 128, 256\}$ and $\sigma'^2 \in \{0.01, 0.04, 0.25, 0.64, 1.0\}$. After searching for the best set of parameters, we obtain $k_* = 64$, $\sigma'^2 = 0.04$ for CIFAR-10 and $k_* = 32$, $\sigma'^2 = 0.04$ for CIFAR-100. The DAE module was updated once at each mini-batch.

Table 10 shows that OmniGAN+LCSA outperforms OmniGAN+DAE, which validates our assumptions on locality-constrained non-linear manifold learning and its ability to deal with the noise and regularization of discriminator.

Model	CIFAR-10			CIFAR-100		
	IS \uparrow	tFID \downarrow	vFID \downarrow	IS \uparrow	tFID \downarrow	vFID \downarrow
OmniGAN	9.70	6.88	10.65	12.78	9.13	13.82
OmniGAN+DAE	10.08	3.89	7.91	13.65	5.52	10.33
OmniGAN+LCSA	10.09	3.29	7.31	13.73	5.12	9.91

Table 10. OmniGAN+DAE vs. OmniGAN+LCSA ($d' = 512$).

G. Fixed β and γ

To verify that metaparameter learning of β and γ works better than setting fixed β and γ , Table 11 shows for the best possible fixed β . For each experiment, $\gamma = \Delta_\gamma \beta$ and $\Delta_\gamma = 1.2$ (same as for learnable experiment). For fixed β and γ , the best results are obtained with ($\beta = 0.4$, $\gamma = 0.48$) for

CIFAR-10 and ($\beta = 0.2, \gamma = 0.24$) for CIFAR-100. Figure 14 provides further ablations.

Method	CIFAR-10			CIFAR-100		
	IS \uparrow	tFID \downarrow	vFID \downarrow	IS \uparrow	tFID \downarrow	vFID \downarrow
Fixed	10.01	4.06	8.03	13.64	5.46	10.29
Learnable	10.09	3.29	7.31	13.73	5.12	9.91

Table 11. Best fixed β and γ vs. best metalearnable β and γ .

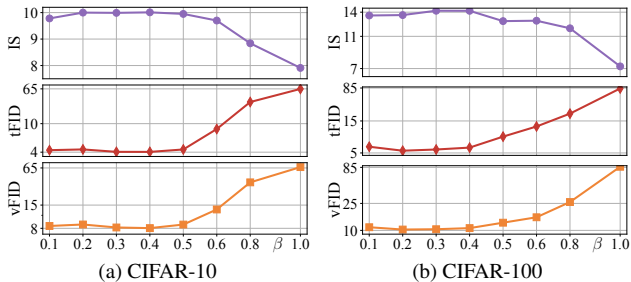


Figure 14. Fixed β and γ , $\gamma = \Delta_\gamma \beta$ where $\Delta_\gamma = 1.2$ (as in the adaptive setting). We show results for several fixed values of β .

H. Illustration of the residual error

We randomly sample images from real dataset on CIFAR-10, and input them into the discriminator. We obtain $\|\mathbf{X}_1 - \tilde{\mathbf{X}}_1\|_F^2$ at the first residual block and normalize for visualization. Figure 15 shows LCSA coder perpetrates larger errors at locations of difficult objects and smaller ones at locations of backgrounds. As Eq. (3).

I. Network architecture and Hyperparameters

Unless specified otherwise, we set $k = 1024$, $\sigma = 1.2$, $\gamma_0 = 0$, $\beta_0 = 0.1$, and $\eta = 0.5$.

CIFAR-10. Below, we experiment with OmniGAN [69] which adopts the architecture of BigGAN [5]. We follow OmniGAN mini-batch size of 32 and train our networks for 500 epochs. To this end, we equip each residual block of the discriminator with the LCSA module. For our experiments on CIFAR-10, we apply weight decays of $1e-4$, $1e-5$ and 0 on generator given $d' = 256, 512, 1024$, weight decay 0 for the discriminator. To update the dictionary, we use the Adam optimizer [24] with learning rate of 0.002. We set Δ_γ equal 1.0, 1.2 and 2.5 given $d' = 256, 512, 1024$. For StyleGAN2+ADA+LCSA, we follow [20] and set $\eta = 0.6$. We set $\Delta_\gamma = 0.05$ due to the architecture differences between StyleGAN2 and BigGAN.

CIFAR-100. We use CIFAR-10 settings but we set the learning rate of DL to 0.0015, $k' = 32$, and weight decays of $5e-4$, $2e-4$, $5e-5$ for discriminators with $d' = 256, 512, 1024$.

ImageNet (64×64). We equip BigGAN and OmniGAN with LCSA (the last 3 blocks $l \in \{3, 4, 5\}$, $d' = 384$). We use the architecture of BigGAN [5]. For OmniGAN and

OmniGAN+LCSA, we set mini-batch size to 256, learning rates of generator/discriminator to $4e-4$, and take 4 discriminator steps per generator step to prevent OmniGAN from diverging. Weight decays are 0 and $2e-5$ for generator and discriminator. For BigGAN, FQGAN and BigGAN+LCSA, we apply settings of FQGAN [67] to set mini-batch size to 512, learning rates of generator and discriminator to $1e-4$ and $4e-4$. We set dictionary learning rate to $1e-3$, $\Delta_\gamma = 1.5$, $k' = 8$. We set $\sigma = 0.8$, $\beta_0 = 0$, $\gamma_0 = 0.1$ given the discriminator does not overfit on this diverse dataset at the early training stage. All models are trained for 200 epochs.

ImageNet (128×128). We only equip OmniGAN with LCSA as OmniGAN consistently outperforms BigGAN. We use setting from ImageNet (64×64) but set dict. learning rate to $2e-4$ and weight decay of discriminator to $5e-6$. The two models are trained for 300 epochs.

Oxford-102 Flowers (256×256). We employ the state-of-the-art model for this dataset, MSG-StyleGAN [18], as our baseline. Following [18], we set the size of mini-batch to 32 while $d' = 512$. We set the number of iteration to $125K$, $k' = 32$, $\Delta_\gamma = 1$, $\eta = 0.7$, dictionary learning rate is $5e-4$, and LCSA is applied to blocks 4 and 5 of discriminator.

FFHQ (256×256). Following [20], we set the mini-batch size to 64, $d' = 512$ and train the networks until the discriminator had seen $25M$ real images. We equip StyleGAN2 with LCSA (the last 4 blocks $l \in \{4, 5, 6, 7\}$). We set $k' = 32$, $\Delta_\gamma = 0.05$, $\eta = 0.9$, dictionary learning rate is $5e-4$.

Table 12 summarizes hyperparameters used in our experiments. We used a very limited range of these parameters (most par. do not change between experiments) *e.g.*, dict. learning rate equals $1e-3$, $1.5e-3$, $2e-3$, $5e-4$ or $2e-4$, β_0 is set to 0 or 0.1, γ_0 is set to 0 or 0.1, Δ_γ is set to 0.05, 1, 1.2, 1.5 or 2.5, σ is set to 0.8 or 1.2, η is set to 0.5, 0.6, 0.7 or 0.9, and k' to 8, 32, or 128.

Table 13 provides number of parameters, FLOPs and the training time for models with/without the LCSA coder.

J. Coding Methods

Algorithms 1 and 2 detail our implementations of Non-Negative Sparse Coding (SC_+) and Sparse Coding (SC).

Algorithm 1 Non-negative Sparse Coding (SC_+).

Input: \mathbf{X}, \mathbf{M} for a given forward pass, κ : the L_1 norm penalty, ι : the number of iterations, ω : the learning rate.

- 1: $\{\alpha_{in} \sim \mathcal{U}(1e-6, 1)\}_{i=1, \dots, k \text{ and } n=1, \dots, N'}$
- 2: $\alpha \leftarrow \left[\frac{\alpha_n}{\|\alpha_n\|_1 + 1e-6} \right]_{n=1}^{N'}$ (concatenate α_n into matrix α)
- 3: **for** $i = 1, \dots, \iota$
- 4: $\Delta \alpha = 2\mathbf{M}^T(\mathbf{X} - \mathbf{M}\alpha) + \kappa$ (gradient computation)
- 5: $\alpha \leftarrow \alpha - \frac{\omega}{(1+i)^{0.3}} \Delta \alpha$ (stochastic gradient descent)
- 6: $\alpha \leftarrow \text{ReLU}(\alpha)$ (reprojection into the feasible set)

Output: α : sparse codes

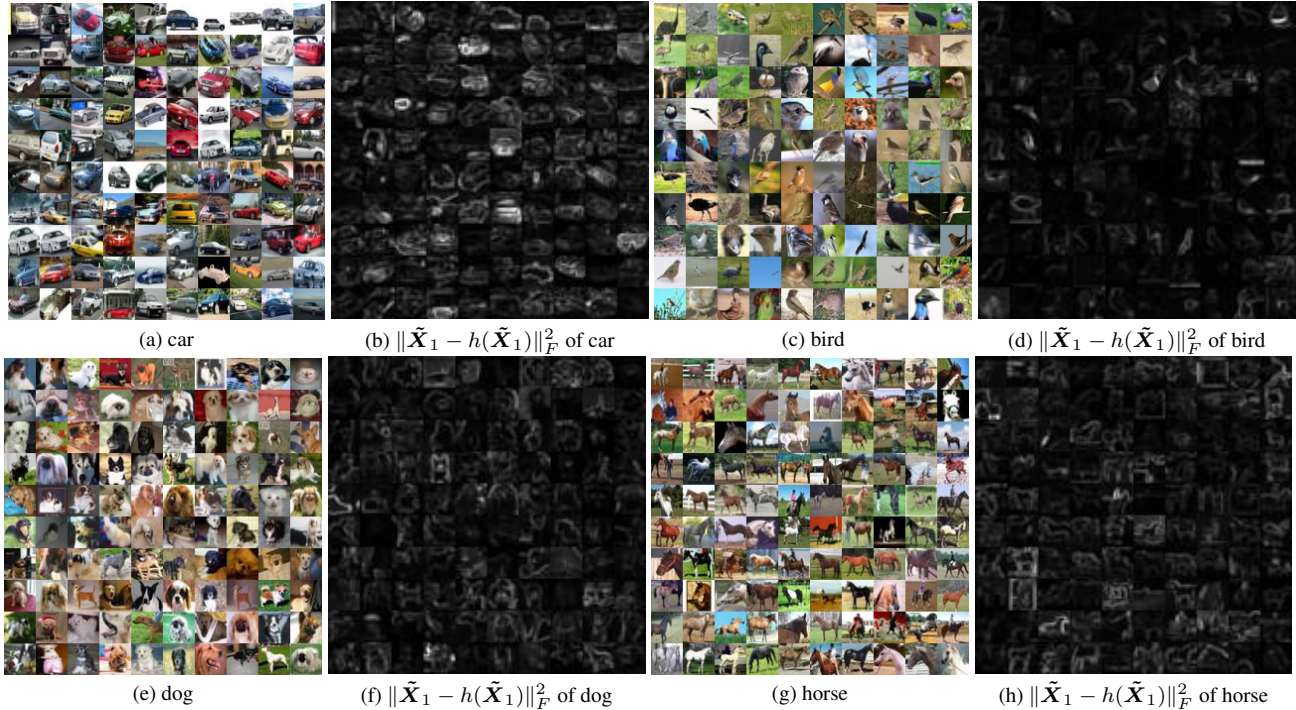


Figure 15. Real samples and the corresponding $\|\tilde{\mathbf{X}}_1 - h(\tilde{\mathbf{X}}_1)\|_F^2$ on CIFAR-10. Whiter pixels correspond to larger $\|\tilde{\mathbf{X}}_1 - h(\tilde{\mathbf{X}}_1)\|_F^2$.

dataset	d'	Model	dict LR	β_0	γ_0	Δ_γ	k'	σ	η	L	GWD	DWD
CIFAR-10	256	OmniGAN+LCSA	2e-3	0.1	0	1.0	128	1.2	0.5	{1,2,3,4}	1e-4	0
		BigGAN	—	—	—	—	—	—	—	—	0	0
	512	BigGAN+LCSA	2e-3	0.1	0	1.2	128	1.2	0.5	{1,2,3,4}	0	0
		OmniGAN	—	—	—	—	—	—	—	—	1e-5	0
		OmniGAN+LCSA	2e-3	0.1	0	1.2	128	1.2	0.5	{1,2,3,4}	1e-5	0
	1024	StyleGAN2+ADA+LCSA	2e-3	0.1	0	0.05	128	1.2	0.6	{1,2,3,4}	0	0
		BigGAN	—	—	—	—	—	—	—	—	0	0
		BigGAN+LCSA	2e-3	0.1	0	2.5	128	1.2	0.5	{1,2,3,4}	0	0
		OmniGAN	—	—	—	—	—	—	—	—	0	0
		OmniGAN+LCSA	2e-3	0.1	0	2.5	128	1.2	0.5	{1,2,3,4}	0	0
CIFAR-100	256	OmniGAN+LCSA	1.5e-3	0.1	0	1.0	32	1.2	0.5	{1,2,3,4}	1e-4	5e-4
		BigGAN	—	—	—	—	—	—	—	—	0	0
	512	BigGAN+LCSA	1.5e-3	0.1	0	1.2	32	1.2	0.5	{1,2,3,4}	0	0
		OmniGAN	—	—	—	—	—	—	—	—	1e-5	2e-4
		OmniGAN+LCSA	1.5e-3	0.1	0	1.2	32	1.2	0.5	{1,2,3,4}	1e-5	2e-4
	1024	BigGAN	—	—	—	—	—	—	—	—	0	0
		BigGAN+LCSA	1.5e-3	0.1	0	2.5	32	1.2	0.5	{1,2,3,4}	0	0
		OmniGAN	—	—	—	—	—	—	—	—	0	5e-5
ImageNet 64 × 64	384	OmniGAN+LCSA	1.5e-3	0.1	0	2.5	32	1.2	0.5	{1,2,3,4}	0	5e-5
		BigGAN	—	—	—	—	—	—	—	—	0	0
		BigGAN+LCSA	1e-3	0	0.1	1.5	8	0.8	0.5	{3,4,5}	0	0
		OmniGAN	—	—	—	—	—	—	—	—	0	2e-5
ImageNet 128 × 128	384	OmniGAN+LCSA	1e-3	0	0.1	1.5	8	0.8	0.5	{3,4,5}	0	2e-5
		OmniGAN	—	—	—	—	—	—	—	—	0	5e-6
Oxford-102 Flowers	512	OmniGAN+LCSA	2e-4	0	0.1	1.5	8	0.8	0.5	{4,5,6}	0	5e-6
		MSG-StyleGAN	—	—	—	—	—	—	—	—	0	0
FFHQ	512	MSG-StyleGAN+LCSA	5e-4	0.1	0	1	32	1.2	0.7	{4,5}	0	0
		StyleGAN2+LCSA	5e-4	0.1	0	0.05	32	1.2	0.9	{4,5,6,7}	0	0

Table 12. Hyperparameter used in our experiments. Abbreviation ‘dict LR’ denotes dictionary learning rate, ‘GWD’ and ‘DWD’ are weight decays of generator and discriminator, respectively.

Dataset	Baseline	GPUs	Baseline	+LCSA
			#Par. / FLOPs Training Time	#Par. / FLOPs Training Time
CIFAR-10	OmniGAN ($d'=512$)	1	32.88M / 11.12G 27h11m	34.97M / 12.04G 30h54m
CIFAR-100	OmniGAN ($d'=512$)	1	33.48M / 11.12G 27h29m	35.57M / 12.04G 30h32m
ImageNet (64×64)	OmniGAN	4	115.69M / 18.84G 3d15h	118.44M / 19.10G 4d01h
ImageNet (128×128)	OmniGAN	4	158.36M / 31.45G 20d03h	162.29M / 31.86G 22d10h
Oxford-102 Flowers	MSG- StyleGAN	4	50.28M / 85.11G 22h46m	51.33M / 86.29G 23h09m
FFHQ	StyleGAN2	4	48.76M / 51.64G 58h42m	50.86M / 53.14G 59h51m

Table 13. Number of parameters/FLOPs (for both generator and discriminator) and training time for models with vs. without the LCSA encoder. Experiments were performed on NVIDIA Tesla V100 GPUs.

Algorithm 2 Sparse Coding (SC).

Input: \mathbf{X}, \mathbf{M} for a given forward pass, κ : the L_1 norm penalty, ν : the number of iterations, ω : the learning rate.

- 1: $\{\alpha_{in} \sim \mathcal{U}(-1, 1)\}_{i=1, \dots, k \text{ and } n=1, \dots, N'}$
- 2: $\alpha_+ = \text{ReLU}(\alpha) + 1e-6$ and $\alpha_- = \text{ReLU}(-\alpha) + 1e-6$
- 3: $\alpha_+ \leftarrow \left[\frac{\alpha_{+,n}}{\|\alpha_{+,n}\|_1 + 1e-6} \right]_{n=1}^{N'}$, $\alpha_- \leftarrow \left[\frac{\alpha_{-,n}}{\|\alpha_{-,n}\|_1 + 1e-6} \right]_{n=1}^{N'}$
- 4: **for** $i=1, \dots, \nu$
- 5: $\Delta\alpha = 2\mathbf{M}^T(\mathbf{X} - \mathbf{M}(\alpha_+ - \alpha_-))$ (compute gradient)
- 6: $\Delta\alpha_+ = \Delta\alpha + \kappa$ and $\Delta\alpha_- = -\Delta\alpha + \kappa$
- 7: $\alpha_+ \leftarrow \alpha_+ - \frac{\omega}{(1+i)^{0.3}} \Delta\alpha_+$ and $\alpha_- \leftarrow \alpha_- - \frac{\omega}{(1+i)^{0.3}} \Delta\alpha_-$
- 8: $\alpha_+ \leftarrow \text{ReLU}(\alpha_+)$ and $\alpha_- \leftarrow \text{ReLU}(\alpha_-)$
- 9: $\alpha \leftarrow \alpha_+ - \alpha_-$

Output: α : sparse codes

Algorithm 3 is our efficient implementation of the Orthogonal Matching Pursuit (OMP) which is based on the batch support of PyTorch. Operations *cat*, *squeeze*, *solve* and *one_hot* are equivalent to PyTorch methods with the same names while \odot is the element-wise multiplication.

Algorithm 4 illustrates that Locality-constrained Linear Coding (LLC) is computed with operations which enjoy the batch support of PyTorch. Once more, operation *solve* is equivalent to the batch-wise linear solver of PyTorch.

Algorithm 5 is a sketch implementation of Locality-constrained Soft Assignment (LCSA). Function *idx_nn* firstly computes distances \mathbf{D} of \mathbf{X} to \mathbf{M} as:

$$\mathbf{D} = [\|\mathbf{x}_1\|_2^2, \dots, \|\mathbf{x}_{N'}\|_2^2] \cdot \mathbf{1}^T + \mathbf{1} \cdot [\|\mathbf{m}_1\|_2^2, \dots, \|\mathbf{m}_k\|_2^2]^T - 2\mathbf{M}^T\mathbf{X}. \quad (20)$$

Subsequently, function *ktop* implemented in PyTorch selects k' indexes of k' smallest distances from \mathbf{D} for each \mathbf{x}_n .

Algorithm 3 Orthogonal Matching Pursuit (OMP).

Input: \mathbf{X}, \mathbf{M} for a given forward pass, τ : the number of non-zero elements (iterations).

- 1: $\mathbf{E} = \mathbf{X}$ (initialize matrix of residuals)
 - 2: $\mathbf{M}^* = \emptyset$ (active dictionary tensor $\mathbf{M}^* \in \mathbb{R}^{d' \times 0 \times N'}$)
 - 3: **for** $i=1, \dots, \tau$
 - 4: $\mathbf{P} = \mathbf{M}^T\mathbf{E}$ (projection of \mathbf{X} onto residual \mathbf{E})
 - 5: $\varphi^i = \text{idx_max}(|\mathbf{P}|)$ (index of maximum coefficient per column)
 - 6: $\mathbf{M}^* = \text{cat}(\mathbf{M}^*, [\mathbf{m}_{\varphi^1}, \dots, \mathbf{m}_{\varphi^i}]); 1)$ (active atoms are added to tensor \mathbf{M}^* so that $\mathbf{M}^* \in \mathbb{R}^{d' \times i \times N'}$)
 - 7: **for** $n=1, \dots, N'$ (this loop is batch solved)
 - 8: $\bar{\mathbf{M}} = \text{squeeze}(\mathbf{M}^*_{:, :, n})$ (dict. $\bar{\mathbf{M}} \in \mathbb{R}^{d' \times i}$ for \mathbf{x}_n)
 - 9: $\alpha_n = \text{solve}(\bar{\mathbf{M}}^T\mathbf{x}_n, \bar{\mathbf{M}}^T\bar{\mathbf{M}})$ (system of linear equations solved by batch solver *torch.solve*(\cdot))
 - 10: $\mathbf{e}_n = \mathbf{x}_n - \bar{\mathbf{M}}\alpha_n$ (residual solved by batch operations at once, that is, $\mathbf{E} \equiv [\mathbf{e}_1, \dots, \mathbf{e}_{N'}]$)
 - 11: $\alpha = \text{one_hot}([\varphi^1, \dots, \varphi^\tau]) \odot [\alpha_1, \dots, \alpha_{N'}]$
- Output:** α : sparse codes
-

Algorithm 4 Locality-constrained Linear Coding (LLC).

Input: \mathbf{X}, \mathbf{M} for a given forward pass, k' : the k' nearest neighbors, ρ : a small reg. constant equal $1e-6$.

- 1: **for** $n=1, \dots, N'$ (this loop is batch solved)
- 2: $\mathbf{C}_n = (\mathbf{M} - \mathbf{1}\mathbf{x}_n^T)(\mathbf{M} - \mathbf{1}\mathbf{x}_n^T)^T$ (so-called data cov.)
- 3: $\alpha_n = \text{solve}(\mathbf{1}, \mathbf{C}_n + \text{diag}(\mathbf{1}) \cdot \rho)$ (matrix left div. by $\mathbf{1}$)
- 4: $\alpha_n \leftarrow \alpha_n / \sum_j \alpha_{jn}$ (normalization)
- 5: $\alpha = [\alpha_1, \dots, \alpha_{N'}]$ (concatenation of vectors α_n into matrix α)

Output: α : locality-constrained linear codes

Algorithm 5 Locality-constrained Soft Assignment (LCSA).

Input: \mathbf{X}, \mathbf{M} for a given forward pass, k' : the k' nearest neighbors, σ : the bandwidth controlling the slope rate.

- 1: **for** $n=1, \dots, N'$ (this loop is batch solved)
- 2: $\varphi = \text{idx_nn}(\mathbf{x}_n; \mathbf{M}, k')$ (k' indexes of k' nearest \mathbf{m}_j of \mathbf{x}_n)
- 3: $\alpha'_n = \alpha'(\mathbf{x}_n; [\mathbf{m}_{\varphi^1}, \dots, \mathbf{m}_{\varphi^{k'}}])$ (SA computed by Eq. (15) on local dictionary)
- 4: $\alpha_n = \pi(\alpha'_n; \varphi, k)$ (deploy coeff. of α'_n to locations φ of k dim. zeroed vector)
- 5: $\alpha = [\alpha_1, \dots, \alpha_{N'}]$ (concat. vectors α_n into matrix α)

Output: α : locality-constrained soft-assigned codes

Algorithm 6 illustrates how we perform the Dictionary Learning (DL) step. While we could solve the Least Squares Problem in the closed-form, we noted that a simple one step of SGD per mini-batch is sufficient to obtain

Algorithm 6 Dictionary Learning (DL).

Input: $\mathbf{X}, \mathbf{M}, \boldsymbol{\alpha}$ for a given forward pass, ω : the learning rate.

- 1: $\{m_{ij} \sim \mathcal{U}(-1, 1)\}_{i=1, \dots, d' \text{ and } j=1, \dots, k}$
- 2: $\mathbf{M} \leftarrow \left[\frac{\mathbf{m}_j}{\|\mathbf{m}_j\|_1 + 1e-6} \right]_{j=1}^k$ (concat. of \mathbf{m}_j into matrix \mathbf{M})
- 3: **for** $i = 1, \dots, \ell$
- 4: $\Delta \mathbf{M} = 2(\mathbf{X} - \mathbf{M}\boldsymbol{\alpha})\boldsymbol{\alpha}^T$ (gradient computation)
- 5: $\mathbf{M} \leftarrow \mathbf{M} - \frac{\omega}{(1+i)^{0.3}} \Delta \mathbf{M}$ (gradient descent)

Output: \mathbf{M} : dictionary atoms

good results. Of course, where needed and/or requested by reviewers, we will refine our claims and proofs further.

K. Generated Images

Figures 16, 17, 18, 19, and 20 show examples of images generated with OminGAN vs. OmniGAN+LCSA after training on CIFAR-10 (32×32), CIFAR-100 (32×32), ImageNet (64×64) (we also include BigGAN & BigGAN+LCSA) and ImageNet (128×128). Figure 21 shows examples of images generated with MSG-StyleGAN vs. MSG-StyleGAN+LCSA after training on Oxford-102 Flowers (256×256). Figures 22 and 23 shows examples of images generated with StyleGAN2 vs. StyleGAN2+LCSA for training on FFHQ (256×256).

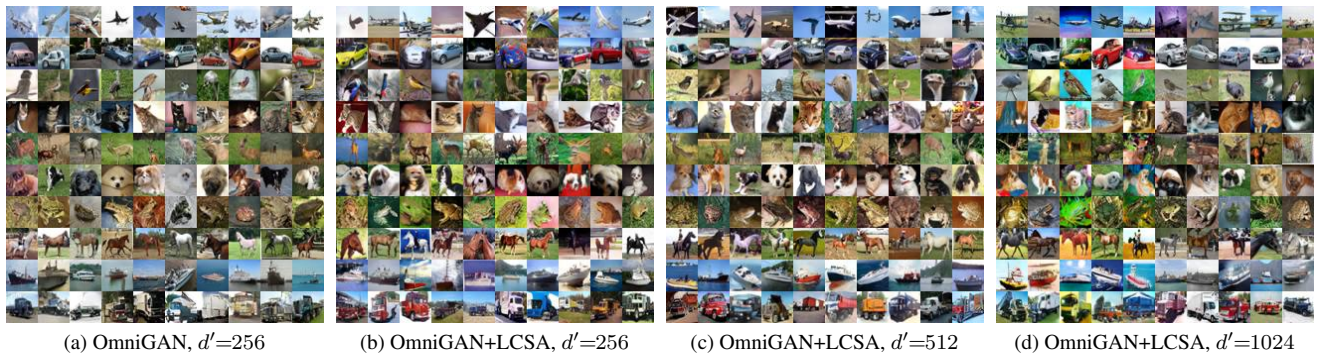
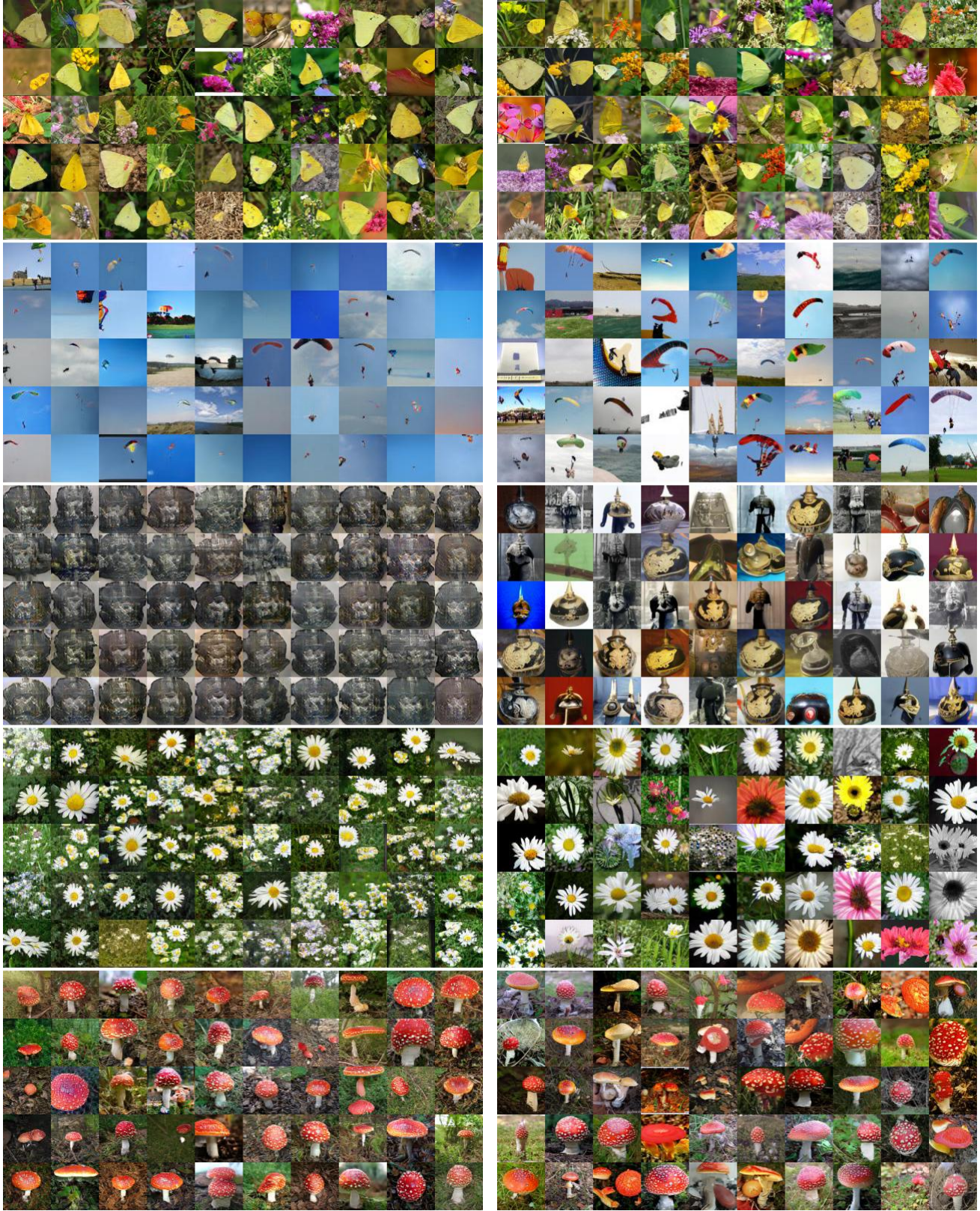


Figure 16. Examples of images generated after training on CIFAR-10 (32×32).



Figure 17. Examples of images generated after training on CIFAR-100 (32×32). Each row contains samples from two classes. We note that OmniGAN+LCSA produces more diverse images than OmniGAN.



(a) BigGAN

(b) BigGAN+LCSA

Figure 18. Images generated by BigGAN and BigGAN+LCSA on ImageNet (64×64). Our BigGAN+LCSA can generate more diverse and realistic images than BigGAN. We also note that the BigGAN has completely failed on class *pickelhaube* (the 3rd row).



(a) OmniGAN

(b) OmniGAN+LCSA

Figure 19. Images generated by OmniGAN and OmniGAN+LCSA on ImageNet (64×64). Our OmniGAN+LCSA produces more diverse and accurate images than OmniGAN alone.

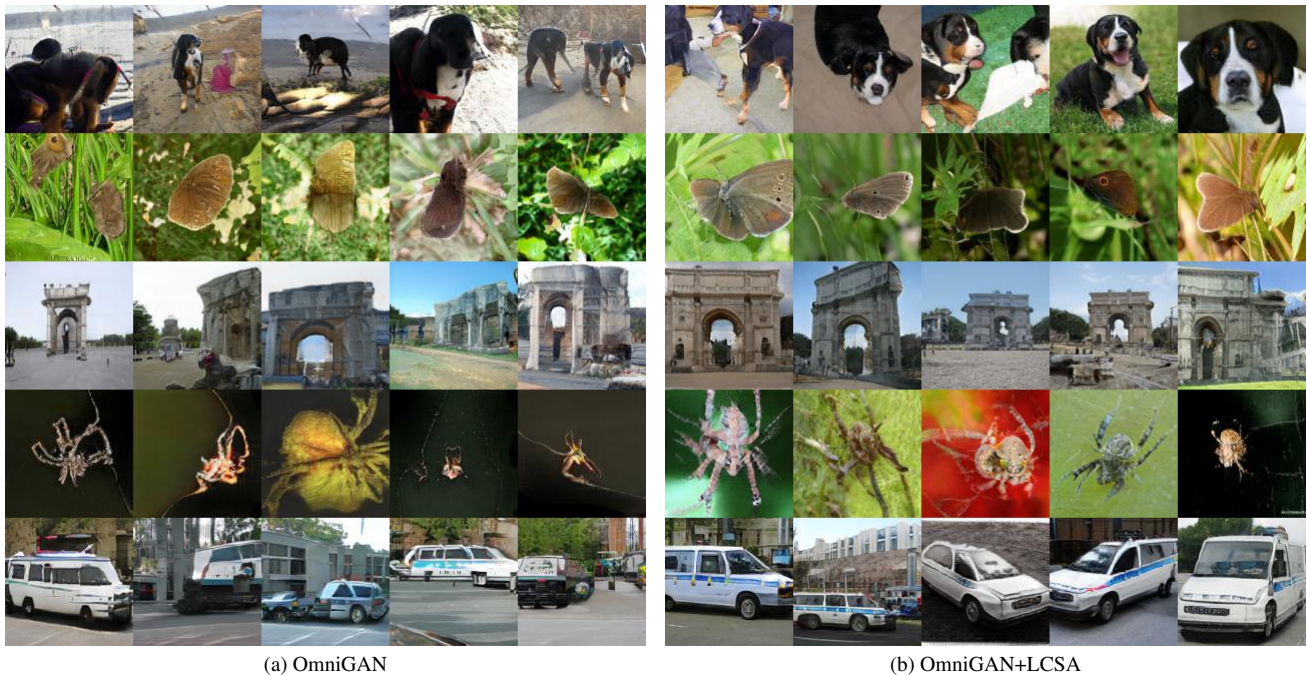


Figure 20. Generated images on ImageNet (128×128) dataset. Our OmniGAN+LCSA can generate more diverse and realistic images than OmniGAN.



Figure 21. Generated images using the mixing of different input noises on Oxford-102 Flowers (256×256). Two sets of images are generated from their respective latent codes (the first row and the first column, respectively). The top left image (red box) is generated using the averaged latent inputs from images in the first row and the first column. The rest of images are generated by averaging the two latent inputs of images chosen from the first row and the first column *i.e.*, $\mathbf{I}_{i,j} = G((\mathbf{z}_{i,1} + \mathbf{z}_{1,j})/2)$. We input the same noise codes to both of the two models. Our MSG-StyleGAN+LCSA can generate more diverse and accurate flowers than MSG-StyleGAN alone.

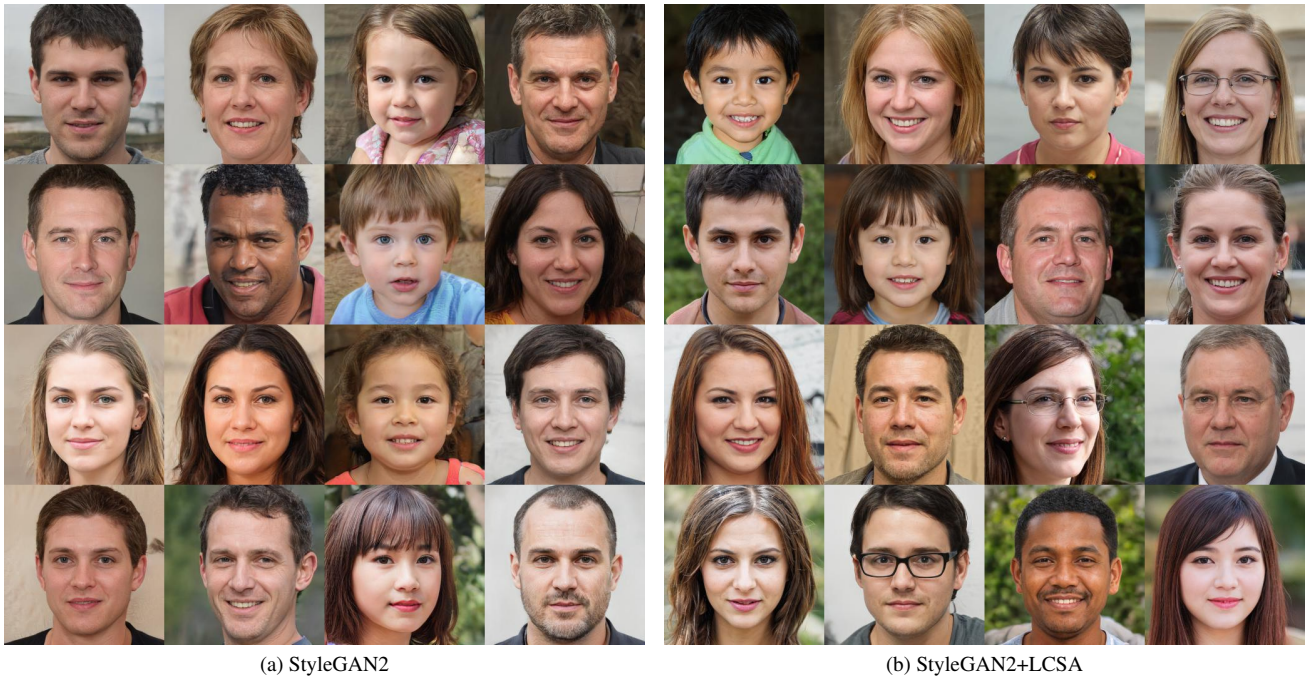


Figure 22. Examples of images generated by training on FFHQ (256×256) 70K dataset with truncation trick using $\psi = 0.5$ [21].



Figure 23. Examples of images generated by training on FFHQ (256×256) 70K dataset without using the truncation trick. We notice that our StyleGAN2+LCSA can generate more realistic images than StyleGAN2 alone.

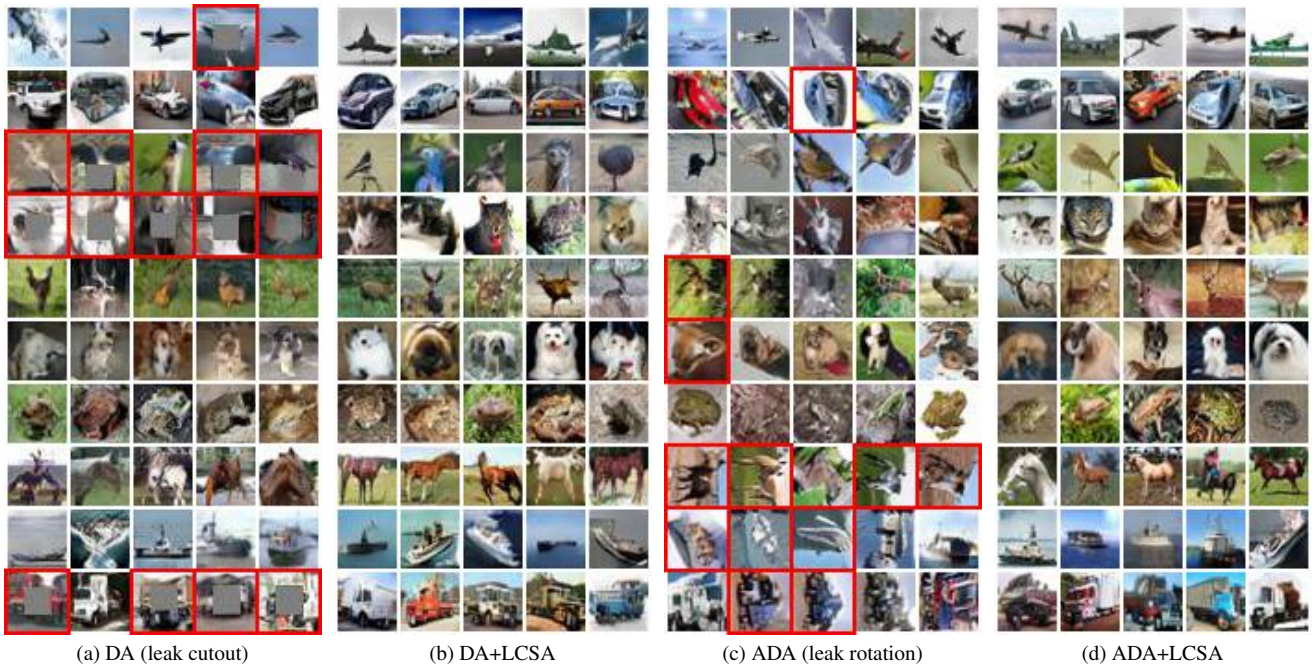


Figure 24. Generated images of different methods limiting overfitting on 10% CIFAR-10 data. **DA leaks the cutout augmentation artifacts.** See images enclosed with red frames. **ADA also leaks the rotation augmentation artifacts.** **Combining LCSA with ADA or DA prevents the leakage of augmentation artifacts.**

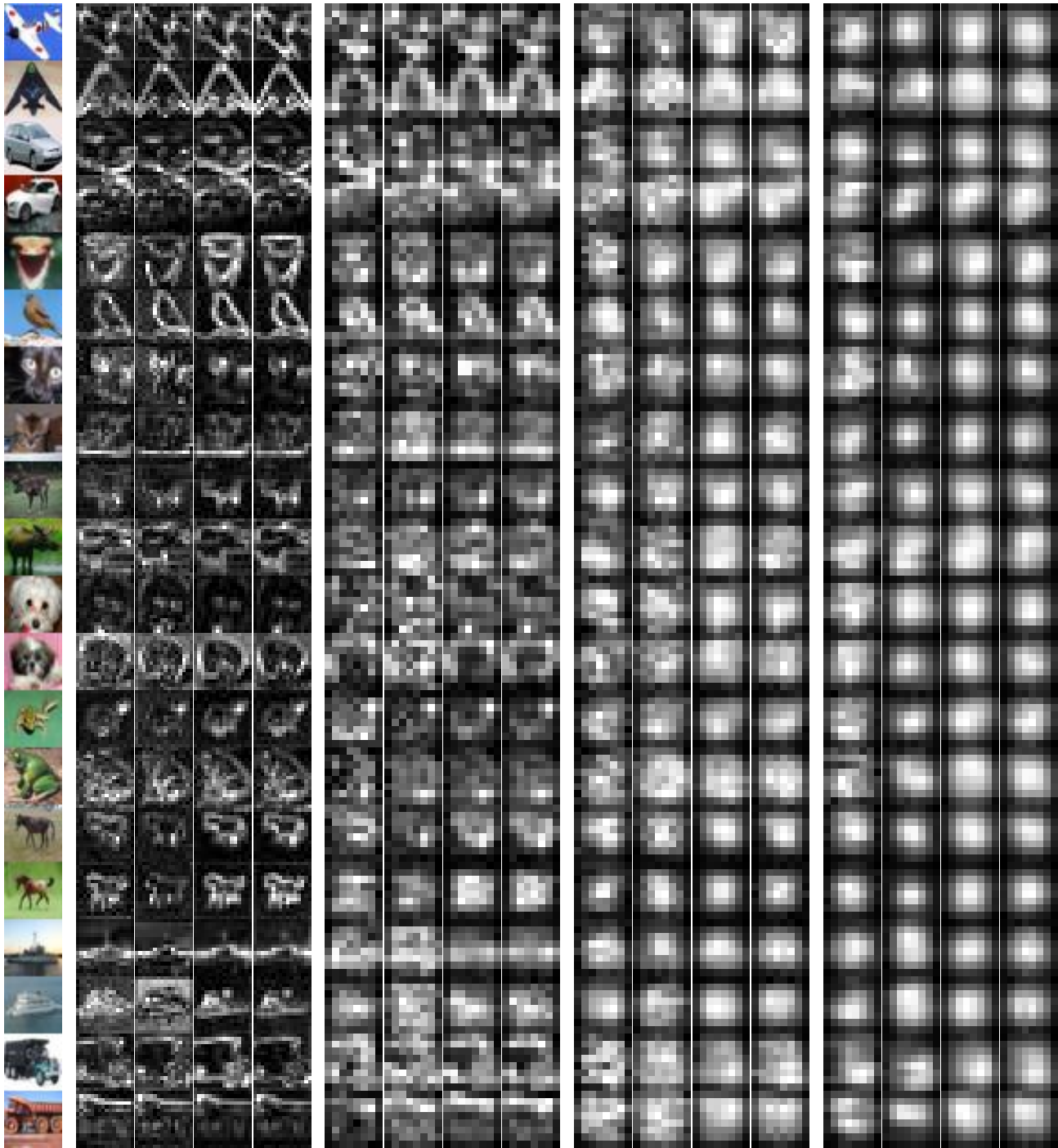


Figure 25. B1(LCSA LLC NNSC OMP), B2(LCSA LLC NNSC OMP), B3(LCSA LLC NNSC OMP), B4(LCSA LLC NNSC OMP). B1, B2, B3 and B4 denote the consecutive blocks of the discriminator. The first column shows the chosen images and remaining columns show the variance of coefficients of each α . Notice that LCSA results in a slightly larger variance on foregrounds and edges of objects than other coders while still maintaining a low variance on fairly basic visual appearances such as uniform backgrounds or simple textures. **We believe this is the example of the ability of LCSA to perform the quantization (backgrounds) vs. the approximate linear coding (foregrounds) trade-off which is controlled with the Lipschitz constant K (de facto σ).**

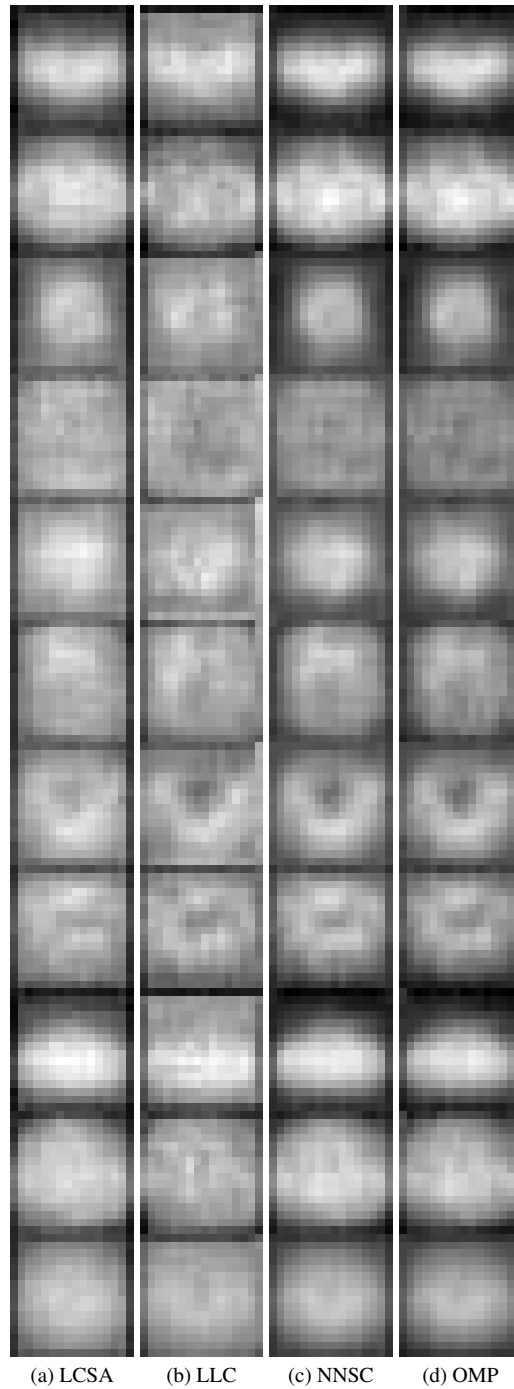


Figure 26. Mean over variance of each α on block B1. The first 10 rows correspond to the mean over variance of coefficients of each α codes of each class, the last row is the mean over variance of coefficients of each α over all classes. Notice that the combined variance of LCSA is again somewhat larger compared to NNSC and OMP but also lower than LLC in the areas of background. This indicates a good trade-off between quantization and reconstruction capacity of LCSA.

L. Sketch Proofs of Claims from Section 5

Below we provide proofs and proof sketches of properties of LCSA. We note that some of mathematics for α' functions is cumbersome, thus we resort to key intuitions where necessary. We use one column display to ease readability of some math formulas. Before embarking on the proofs, we develop key quantities about α' . Since it lives on the probability simplex, we compute Shannon's entropy $S(\cdot) = -\mathbb{E}_{\alpha'}[\log \alpha']$ of α' (α being α' composed with a linear operator, its fundamental geometric properties follow from α'). We recall

$$\alpha'(\mathbf{x}; \mathbf{M}, \sigma) = \frac{1}{Z(\mathbf{x}; \mathbf{M}, \sigma)} \left[e^{-\frac{1}{2\sigma^2} \|\mathbf{x} - \mathbf{m}_1\|_2^2}, \dots, e^{-\frac{1}{2\sigma^2} \|\mathbf{x} - \mathbf{m}_k\|_2^2} \right]^T \quad (21)$$

After some algebra that we skip for readability, we arrive at the statistical form of the gradient ∇S and Hessian HS at any \mathbf{x} (skipped from notations for readability)

$$\begin{aligned} \nabla S(\mathbf{x}) &= \frac{\mathbb{E}_p[\delta]}{2\sigma^2} \cdot (\mathbb{E}_q[\mathbf{m}] - \mathbb{E}_p[\mathbf{m}]), \\ HS(\mathbf{x}) &= \frac{\mathbb{E}_p[\delta]}{2\sigma^4} \cdot \mathbb{E}_q[(\mathbf{m} - \mathbb{E}_p[\mathbf{m}])(\mathbf{m} - \mathbb{E}_p[\mathbf{m}])^T] - \frac{2 + \mathbb{E}_p[\delta]}{2\sigma^4} \cdot \mathbb{E}_p[(\mathbf{m} - \mathbb{E}_p[\mathbf{m}])(\mathbf{m} - \mathbb{E}_p[\mathbf{m}])^T], \end{aligned}$$

where expectations are with respect to dictionary's columns, and for any such column \mathbf{m}_i , we let $\delta_i = \frac{\|\mathbf{x} - \mathbf{m}_i\|_2^2}{\sigma^2}$ and p, q are the distributions in the k -dim probability simplex with $p_i \propto \exp\left(-\frac{\|\mathbf{x} - \mathbf{m}_i\|_2^2}{2\sigma^2}\right)$ and $q_i \propto p_i \delta_i$. From the shape operator of the entropy (see *e.g.* [41]),

$$sS = -\frac{1}{\sqrt{1 + \|\nabla S\|_2^2}} \cdot (\mathbf{I} + \nabla S \nabla S^T)^{-1} HS,$$

we deduce the general formula for the mean curvature of S (using Sherman-Morrison Lemma to get rid of the inverse and properties of the trace),

$$\begin{aligned} hS &= \frac{1}{k \sqrt{1 + \|\nabla S\|_2^2}} \cdot \text{tr} \left(\left(\mathbf{I} - \frac{1}{1 + \|\nabla S\|_2^2} \cdot \nabla S \nabla S^T \right) \cdot -HS \right) \\ &= \frac{1}{k(1 + \|\nabla S\|_2^2)^{\frac{3}{2}}} \cdot [\nabla S^T HS \nabla S - \|\nabla S\|_2^2 \cdot \text{tr}(HS) - \text{tr}(HS)]. \end{aligned}$$

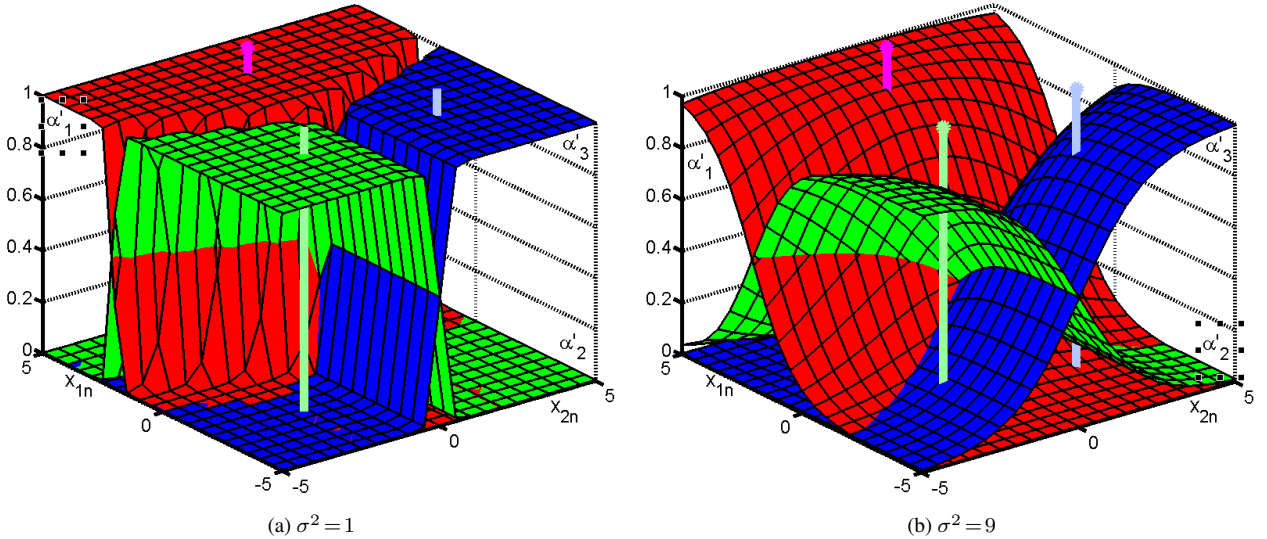


Figure 27. Illustration of α of LCSA. Two-dimensional anchors $[\mathbf{m}_1, \mathbf{m}_2, \mathbf{m}_3]$ were used (three poles). LCSA was applied w.r.t. $\mathbf{x} \in [-5, 5]^2$. Responses $\alpha' = [\alpha'_1, \alpha'_2, \alpha'_3]$ are given in three colors.

For any vector \mathbf{a} on the k -dim probability simplex, let us use the shorthand $\boldsymbol{\mu}_a = \mathbb{E}_a[\mathbf{m}]$. Let us define, for any two such vectors \mathbf{a}, \mathbf{b} ,

$$J(\mathbf{a}, \mathbf{b}) = \mathbb{E}_a[\|\mathbf{m}\|_2^2] \|\boldsymbol{\mu}_b - \boldsymbol{\mu}_a\|_2^2 - \mathbb{E}_a[(\boldsymbol{\mu}_a - \boldsymbol{\mu}_b)^T \mathbf{m}]^2 + (\boldsymbol{\mu}_b^\top \boldsymbol{\mu}_a)^2 - \|\boldsymbol{\mu}_a\|_2^2 \|\boldsymbol{\mu}_b\|_2^2. \quad (22)$$

Notice that Cauchy-Schwartz inequality brings

$$\mathbb{E}_a[(\boldsymbol{\mu}_a - \boldsymbol{\mu}_b)^T \mathbf{m}]^2 \leq \mathbb{E}_a[\|\mathbf{m}\|_2^2] \|\boldsymbol{\mu}_b - \boldsymbol{\mu}_a\|_2^2, \quad (23)$$

$$(\boldsymbol{\mu}_b^\top \boldsymbol{\mu}_a)^2 \leq \|\boldsymbol{\mu}_a\|_2^2 \|\boldsymbol{\mu}_b\|_2^2, \quad (24)$$

so we get a useful interval to which $J(\mathbf{a}, \mathbf{b})$ belongs: $J(\mathbf{a}, \mathbf{b}) \in \mathbb{I}(\mathbf{x}; \mathbf{M}, \sigma)$ with:

$$\mathbb{I}(\mathbf{x}; \mathbf{M}, \sigma) = \left[-(\|\boldsymbol{\mu}_a\|_2^2 \|\boldsymbol{\mu}_b\|_2^2 - (\boldsymbol{\mu}_b^\top \boldsymbol{\mu}_a)^2), \mathbb{E}_a[\|\mathbf{m}\|_2^2] \|\boldsymbol{\mu}_b - \boldsymbol{\mu}_a\|_2^2 - \mathbb{E}_a[(\boldsymbol{\mu}_a - \boldsymbol{\mu}_b)^T \mathbf{m}]^2 \right], \quad (25)$$

and we note that those Cauchy-Schwartz inequalities (23), (24) also yield

$$0 \in \mathbb{I}(\mathbf{x}; \mathbf{M}, \sigma). \quad (26)$$

After some more derivations, we arrive at the expression

$$\begin{aligned} hS &= \frac{\left\{ \begin{array}{l} \left(\frac{\mathbb{E}_p[\delta]}{2\sigma^2} \right)^2 \cdot \frac{2 + \mathbb{E}_p[\delta]}{2\sigma^4} \cdot (\mathbb{E}_p[\|\mathbf{m}\|_2^2] \|\boldsymbol{\mu}_q - \boldsymbol{\mu}_p\|_2^2 - \mathbb{E}_p[(\boldsymbol{\mu}_p - \boldsymbol{\mu}_q)^T \mathbf{m}]^2) + (\boldsymbol{\mu}_q^\top \boldsymbol{\mu}_p)^2 - \|\boldsymbol{\mu}_p\|_2^2 \|\boldsymbol{\mu}_q\|_2^2 \\ - \left(\frac{\mathbb{E}_p[\delta]}{2\sigma^2} \right)^2 \cdot \frac{\mathbb{E}_p[\delta]}{2\sigma^4} \cdot (\mathbb{E}_q[\|\mathbf{m}\|_2^2] \|\boldsymbol{\mu}_q - \boldsymbol{\mu}_p\|_2^2 - \mathbb{E}_q[(\boldsymbol{\mu}_p - \boldsymbol{\mu}_q)^T \mathbf{m}]^2) + (\boldsymbol{\mu}_p^\top \boldsymbol{\mu}_q)^2 - \|\boldsymbol{\mu}_p\|_2^2 \|\boldsymbol{\mu}_q\|_2^2 \end{array} \right\}}{k \left(1 + \left(\frac{\mathbb{E}_p[\delta]}{2\sigma^2} \right)^2 \cdot \|\boldsymbol{\mu}_q - \boldsymbol{\mu}_p\|_2^2 \right)^{\frac{3}{2}}} \\ &= \frac{(\mathbb{E}_p[\delta])^2}{k\sigma^2} \cdot \frac{(2 + \mathbb{E}_p[\delta]) \cdot J(\mathbf{p}, \mathbf{q}) - \mathbb{E}_p[\delta] \cdot J(\mathbf{q}, \mathbf{p})}{(4\sigma^4 + (\mathbb{E}_p[\delta])^2 \cdot \|\boldsymbol{\mu}_q - \boldsymbol{\mu}_p\|_2^2)^{\frac{3}{2}}}. \end{aligned} \quad (27)$$

We are now ready to develop the proofs (or proof sketches) to our various Claims:

Proof of Claim 1. Since

$$\frac{1}{(z + a)^{\frac{3}{2}}} = \frac{1}{a^{\frac{3}{2}}} - \frac{3z}{2a^{\frac{5}{2}}} + o(z),$$

we get the Taylor expansion of hS in (27) as $\sigma \rightarrow 0$ ($Q, R \neq 0$):

$$hS = \frac{Q}{k\sigma^2} + \sigma^2 R + o(\sigma^2).$$

So hS diverges at rate $1/\sigma^2$ as $\sigma \rightarrow 0$, which shows that the entropy's support approaches a vertex of the probability simplex (where its curvature is maximal) and we get the HA solution.

Proof of Claim 2. We analyze cases for which $hS \rightarrow 0$. Looking at (27), we see several scenarii: (i) $\mathbb{E}_p[\delta]$ is small. This only happens when all the dictionary columns are close to each other and \mathbf{x} is close to them. In Fig. 27, this would amount to brings all poles close to each other and would thus bring regions of linearity, i.e. the intersection of Voronoi cells, close to each other. Another case, (ii), is when $\|\boldsymbol{\mu}_q - \boldsymbol{\mu}_p\|_2 \leq \epsilon$ with a decreasing ϵ , because then both bounds of interval $\mathbb{I}(\mathbf{x}; \mathbf{M}, \sigma)$ are $O(\epsilon^2)$ and so the mean curvature vanishes as well. Looking at $\boldsymbol{\mu}_q - \boldsymbol{\mu}_p$, one can see that the norm of their differences vanishes in particular when there are two sets of dictionary anchors, one which are far away from \mathbf{x} , and thus with low weight on both p and q , and a second set, closer to \mathbf{x} and such that all norms $\|\mathbf{m} - \mathbf{x}\|_2$ are approximately constant, which precisely mean that \mathbf{x} is close to the center of the Voronoi cell defined by those anchors. There is also a simple visual argument: Figure 27 shows that the rapid slope change takes place at $\boldsymbol{\mu}_{12} = \frac{1}{2}(\mathbf{m}_1 + \mathbf{m}_2)$, $\boldsymbol{\mu}_{13} = \frac{1}{2}(\mathbf{m}_1 + \mathbf{m}_3)$, $\boldsymbol{\mu}_{23} = \frac{1}{2}(\mathbf{m}_2 + \mathbf{m}_3)$ and $\boldsymbol{\mu}_{123} = \frac{1}{3}(\mathbf{m}_1 + \mathbf{m}_2 + \mathbf{m}_3)$.

In fact, maximizing over the absolute value of derivatives of each α'_i w.r.t. \mathbf{x} , that is, $\operatorname{argmax}_{\mathbf{x}} \left| \frac{\partial \alpha'_i}{\partial \mathbf{x}'} \right|$, yields maximum at

locations $\boldsymbol{\mu}_{\Lambda(k')}$, where operator argmax_t returns top $t = |\Lambda|$ maxima, Λ returns all possible ordered subsets of non-zero sizes of anchor indexes $i = 1, \dots, k'$ e.g., for $k' = 3$ we have $\{(1, 2), (1, 3), (2, 3), (1, 2, 3)\} = \Lambda(3)$. At $\{\boldsymbol{\mu}_{\Lambda(k')}\}$ locations, the maximum indicates the largest slope changes which coincide with the linear slope regime of sigmoid function.

Proof of Claim 3. To this end, we seek the stationary points of $\epsilon^2 = \|\mathbf{x} - \sum_k \mathbf{m}_k \alpha_k(\mathbf{x}; \mathbf{M}, \sigma)\|_2^2$ where

$$\alpha_k = \frac{\exp(-\|\mathbf{x} - \mathbf{m}_k\|^2/2\sigma^2)}{Z},$$

just as in (21) and \mathbf{m}_k are dictionary atoms defining the Voronoi cell of \mathbf{x} . By setting $\frac{\partial \epsilon^2}{\partial \sigma} = 0$ we obtain

$$-\frac{2}{\sigma^3}(\mathbf{x} - \mathbf{M}\boldsymbol{\alpha}(x)) \left(\sum_i \mathbf{m}_i \alpha_i(\mathbf{x}) (\|\mathbf{x} - \mathbf{m}_i\|_2^2 - c) \right) = 0$$

where $c = \sum_k \|\mathbf{x} - \mathbf{m}_k\|_2^2 \alpha_k(x)$. It is trivial to see that the first maximum is at the stationary point $\sigma = \infty$. Moreover, for $\sigma = 0$ we have also the stationary point as

$$-\frac{2}{\sigma^3}(\mathbf{x} - \mathbf{M}\boldsymbol{\alpha}(x)) \left(\sum_i \mathbf{m}_i \alpha_i(\mathbf{x}) (\|\mathbf{x} - \mathbf{m}_i\|_2^2 - c) \right) = 0 \quad (28)$$

$$-\frac{2}{\sigma^3}(\mathbf{x} - \mathbf{M}\boldsymbol{\alpha}(x)) \left(\left(\sum_i \mathbf{m}_i \alpha_i(\mathbf{x}) \|\mathbf{x} - \mathbf{m}_i\|_2^2 \right) - \left(\sum_i \mathbf{m}_i \alpha_i^2(\mathbf{x}) \|\mathbf{x} - \mathbf{m}_i\|_2^2 \right) \right) = 0 \quad (29)$$

because if $\sigma = 0$ then

$$\sum_i \mathbf{m}_i \alpha_i(\mathbf{x}) \|\mathbf{x} - \mathbf{m}_i\|_2^2 = \sum_i \mathbf{m}_i \alpha_i^2(\mathbf{x}) \|\mathbf{x} - \mathbf{m}_i\|_2^2. \quad (30)$$

The last condition follows from the simplification of c due to the fact that for $\sigma = 0$, $\boldsymbol{\alpha}$ codes obey the Hard Assignment, that is only one coefficient of $\boldsymbol{\alpha}$ is equal one, the rest are equal zero.

It is easy to see the other stationary point occurs if $\mathbf{x} = \mathbf{M}\boldsymbol{\alpha}(x)$ which we already identified as the case of perfect reconstruction.

The last set of stationary points needs to satisfy

$$\sum_i \mathbf{m}_i \alpha_i(\mathbf{x}) \left(d_i^2 - \sum_k d_k^2 \alpha_k(\mathbf{x}) \right) = 0,$$

where $d_i^2 = \|\mathbf{x} - \mathbf{m}_i\|_2^2$ (for d_k^2 just substitute k in place of i), and for these points we have checked via simulations that they yield the minimum reconstruction error.

Proof of Claim 4 (Lipschitz condition). Define $\mathbf{y} = \mathbf{M}\boldsymbol{\alpha}(x) = h(\mathbf{x})$, where $\boldsymbol{\alpha}$ is the LCSA mapping. The task is to compute the Jacobian matrix $\partial \mathbf{y} / \partial \mathbf{x}$. Therefore we compute $\partial y_i / \partial x_j$.

We have

$$\mathbf{y} = \sum_k \mathbf{m}_k \alpha_k \quad (31)$$

where

$$\alpha_k = \frac{\exp(-\|\mathbf{x} - \mathbf{m}_k\|^2/2\sigma^2)}{Z}$$

and Z is defined so that $\sum_k \alpha_k = 1$. From this we get

$$\begin{aligned} \frac{\partial(\alpha_k Z)}{\partial x_j} &= \exp(-\|\mathbf{x} - \mathbf{m}_k\|^2/2\sigma^2) (m_{kj} - x_j) / \sigma^2 \\ &= Z \alpha_k (m_{kj} - x_j) / \sigma^2, \end{aligned} \quad (32)$$

where m_{kj} is the j -th component of \mathbf{m}_k .

In addition, since $Z = \sum_k \alpha_k Z$, summing (32) we get

$$\frac{\partial Z}{\partial x_j} = \sum_k Z \alpha_k (m_{kj} - x_j) / \sigma^2. \quad (33)$$

From (31) we have,

$$y_i = \frac{\sum_k m_{ki} (\alpha_k Z)}{Z},$$

where we have multiplied top and bottom by Z , for convenience. We differentiate this as a quotient, using (32) and (33), giving

$$\begin{aligned} \sigma^2 \frac{\partial y_i}{\partial x_j} &= \frac{Z (\sum_k m_{ki} Z \alpha_k (m_{kj} - x_j)) - (\sum_k m_{ki} (\alpha_k Z)) (\sum_k Z \alpha_k (m_{kj} - x_j))}{Z^2} \\ &= \sum_k m_{ki} \alpha_k (m_{kj} - x_j) - \left(\sum_k m_{ki} \alpha_k \right) \left(\sum_k \alpha_k (m_{kj} - x_j) \right) && \text{cancelling } Z^2 \\ &= \sum_k m_{ki} \alpha_k (m_{kj} - x_j) - \left(\sum_k m_{ki} \alpha_k \right) \left(\left(\sum_k \alpha_k m_{kj} \right) - x_j \right) && \text{since } \sum_k \alpha_k x_j = x_j \\ &= \sum_k m_{ki} \alpha_k m_{kj} - \left(\sum_k m_{ki} \alpha_k \right) \left(\sum_k \alpha_k m_{kj} \right) && \text{cancelling } x_j \\ &= \sum_k \alpha_k m_{ki} m_{kj} - y_i y_j. \end{aligned} \quad (34)$$

Finally, writing $\tilde{m}_k = m_k - \mathbf{y}$, this gives

$$\frac{\partial y_i}{\partial x_j} = \frac{1}{\sigma^2} \sum_k \alpha_k \tilde{m}_{ki} \tilde{m}_{kj}. \quad (35)$$

This shows the interesting fact that the Jacobian is symmetric positive-semidefinite, and can be written in a way depending only on $\mathbf{y} = h(\mathbf{x})$, but not on \mathbf{x} directly.

A further interesting result can be derived from (35). Let $d\mathbf{x}$ be an infinitesimal change in \mathbf{x} . The corresponding infinitesimal change in \mathbf{y} is computed by

$$\begin{aligned} dy_i &= \frac{\partial y_i}{\partial \mathbf{x}} d\mathbf{x} \\ &= \sum_j \frac{\partial y_i}{\partial x_j} dx_j \\ &= \frac{1}{\sigma^2} \sum_k \alpha_k \tilde{m}_{ki} \sum_j \tilde{m}_{kj} dx_j && \text{after interchanging summation order} \\ &= \frac{1}{\sigma^2} \sum_k \alpha_k \tilde{m}_{ki} \langle \tilde{m}_k, d\mathbf{x} \rangle. \end{aligned}$$

Now, if $d\mathbf{x}$ is perpendicular to the simplex Δ , then it is perpendicular to each \tilde{m}_k , so the inner product vanishes. Consequently, dy_i vanishes for all i , and $d\mathbf{y} = 0$. This shows that if \mathbf{x} varies in a direction perpendicular to the simplex, then the value of $\mathbf{y} = h(\mathbf{x})$ does not change. This is a verification of the fact that $h(\mathbf{x})$ is constant on *fibres* perpendicular to the simplex Δ .

The formula (34) can be written neatly using matrices. Suppose that M is the matrix with columns m_k . Then we have

$$\begin{aligned} \sigma^2 \frac{\partial \mathbf{y}}{\partial \mathbf{x}} &= M \text{diag}(\alpha) M^T - \mathbf{y} \mathbf{y}^T \\ &= M (\text{diag}(\alpha) - \alpha \alpha^T) M^T, \end{aligned} \quad (36)$$

Lipschitz condition – L_1 . A Lipschitz constant for a function $\mathbf{y} = h(\mathbf{x})$ with respect to some norm $\|\cdot\|$ is a constant K such that

$$\|\mathbf{y} - \mathbf{y}'\| \leq K \|\mathbf{x} - \mathbf{x}'\| .$$

For a differentiable function a Lipschitz constant for the L_1 vector norm is given by

$$K = \max_j \|\partial \mathbf{y} / \partial x_j\|_1$$

evaluated over the domain of the function (a single Voronoi cell for instance).

From (35) we have

$$\begin{aligned} K &= (1/\sigma^2) \max_j \left\| \sum_k \alpha_k \tilde{\mathbf{m}}_k \tilde{m}_{kj} \right\|_1 \\ &\leq (1/\sigma^2) \max_j \sum_k \|\alpha_k \tilde{\mathbf{m}}_k \tilde{m}_{kj}\|_1 && \text{triangle inequality} \\ &\leq (1/\sigma^2) \sum_k \max_j \|\alpha_k \tilde{\mathbf{m}}_k \tilde{m}_{kj}\|_1 && \text{interchanging max and sum} \\ &= (1/\sigma^2) \sum_k \max_j \alpha_k |\tilde{m}_{kj}| \|\tilde{\mathbf{m}}_k\|_1 && \text{taking scalars outside the norm} \\ &= (1/\sigma^2) \sum_k \alpha_k \|\tilde{\mathbf{m}}_k\|_1 \max_j |\tilde{m}_{kj}| && \text{taking terms outside max} \\ &= (1/\sigma^2) \sum_k \alpha_k \|\tilde{\mathbf{m}}_k\|_1 \|\tilde{\mathbf{m}}_k\|_\infty \\ &\leq (1/\sigma^2) \max_k \|\tilde{\mathbf{m}}_k\|_1 \|\tilde{\mathbf{m}}_k\|_\infty && \text{since } \sum_k \alpha_k = 1 \end{aligned}$$

This leads to

$$K \leq \frac{\max_k \|\tilde{\mathbf{m}}_k\|_1^2}{\sigma^2}$$

Since $\tilde{\mathbf{m}}_k = \mathbf{m}_k - \mathbf{y}$ and \mathbf{y} can vary, we see that $\|\tilde{\mathbf{m}}_k\|^2 \leq D^2$ where D (with respect to the given norm) is the diameter of the simplex with vertices \mathbf{m}_k . (The diameter of a set is the supremum of distances between two points in the set.) This gives finally

$$K \leq \frac{D^2}{\sigma^2} .$$

This will be true for any norm that is greater than the ∞ -norm for all points. However, it therefore applies to any norm that is greater than a multiple of the ∞ -norm. Therefore we can conclude Proposition 2.4 as follows.

Proposition 2.4: For any norm $\|\cdot\|$ on \mathbb{R}^d equivalent to the 2-norm, a Lipschitz constant for the LCSA mapping on a given Voronoi region is given by

$$K = \frac{D^2}{\sigma^2}$$

where D is the diameter of the simplex Δ .

Lipschitz condition – L_2 . For the L_2 norm a Lipschitz constant is given by

$$K = \max_{\|\mathbf{v}\|} \frac{\|J\mathbf{v}\|}{\|\mathbf{v}\|}$$

where \mathbf{v} is a vector and $J = \partial y_i / \partial x_j$ is the Jacobian. In the case where J is symmetric positive definite (such as in the present case), this is equal to

$$K = \max_{\|\mathbf{v}\|=1} \mathbf{v}^T J \mathbf{v} . \tag{37}$$

With $J = \partial y_i / \partial x_j = \sum_k \alpha_k \tilde{m}_{ki} \tilde{m}_{kj} / \sigma^2$ as in (35) this becomes

$$\begin{aligned} \mathbf{v}^T J \mathbf{v} &= (1/\sigma^2) \sum_k \alpha_k \langle \tilde{\mathbf{m}}_k, \mathbf{v} \rangle^2 \\ &\leq (1/\sigma^2) \max_k \langle \tilde{\mathbf{m}}_k, \mathbf{v} \rangle^2. \end{aligned}$$

This quantity is maximized, over vectors \mathbf{v} of norm 1 when $\mathbf{v} = \arg \max_k \|\tilde{\mathbf{m}}_k\|$ (up to scale), in which case it is equal to $\max_k \|\tilde{\mathbf{m}}_k\|^2 / \sigma^2$. This shows that when $\|\mathbf{v}\| = 1$,

$$\begin{aligned} \mathbf{v}^T J \mathbf{v} &\leq \max_k \|\tilde{\mathbf{m}}_k\|^2 / \sigma^2 \\ &\leq D^2 / \sigma^2. \end{aligned} \tag{38}$$

This shows that the same Lipschitz constant $K = D^2 / \sigma^2$ holds for the L_2 as for the L_1 Lipschitz condition.

Proof of Claim 5. The LCSA encoding $M\alpha(\mathbf{x})$ is non-continuous at the boundaries of the Voronoi regions simply because the set of k' nearest neighbor anchors of \mathbf{x} changes as \mathbf{x} crosses from one Voronoi region to another the Voronoi region.

Proof of Claim 7. We penalise the spectral norm of Jacobian matrix $\left\| \frac{\partial M\alpha(\mathbf{x})}{\partial \mathbf{x}} \right\|_2 = K$ via de facto controlling the Lipschitz constant $K = D^2 / \sigma^2$ because this is shown in (37) and (38).

Claims 1–8 highlight that LCSA can perform the feature quantization in some regions of the feature space (proximity of dictionary atoms), as well as it can perform the approximate linear coding akin to linear coding methods (the proximity of the mean of atoms of Voronoi cell). The Lipschitz constant highlights that our σ controls denoising achieved via LCSA due to the mechanism akin to DAE (whose denoising effect is controlled by its σ'). Our blocks in the GAN discriminator can guide the dictionary atoms and conv. features towards quantization or reconstruction with higher linear fidelity, also selecting some intermediate denoising hypothesis as the Lipschitz constant poses the upper bound controlling denoising effect.